



## Inorganic nanotubes†

C. N. R. Rao<sup>\*a,b</sup> and Manashi Nath<sup>a,b</sup>

<sup>a</sup> CSIR Centre for Excellence in Chemistry and Chemistry and Physics of Materials Unit, Jawaharlal Nehru Centre for Advanced Scientific Research, Jakkur P.O., Bangalore, 560 064, India. E-mail: cnrrao@jncasr.ac.in

<sup>b</sup> Solid State and Structural Chemistry Unit, Indian Institute of Science, Bangalore, 560 012, India

Received 13th September 2002, Accepted 14th November 2002

First published as an Advance Article on the web 2nd December 2002

Carbon nanotubes were discovered in 1991. It was soon recognized that layered metal dichalcogenides such as MoS<sub>2</sub> could also form fullerene and nanotube type structures, and the first synthesis was reported in 1992. Since then, a large number of layered chalcogenides and other materials have been shown to form nanotubes and their structures investigated by electron microscopy. Inorganic nanotubes constitute an important family of nanostructures with interesting properties and potential applications. In this article, we discuss the progress made in this novel class of inorganic nanomaterials.

### 1. Introduction

In 1991, Iijima<sup>1</sup> observed some unusual structures of carbon under the transmission electron microscope wherein the graphene sheets had rolled and folded onto themselves to form hollow structures. Iijima called them *nanotubes* of carbon which consisted of several concentric cylinders of graphene sheets. Graphene sheets are hexagonal networks of carbon and these layers get stacked one above the other in the *c*-direction to form bulk graphite. Following the initial discovery, intense research has been carried out on carbon nanotubes (CNTs).<sup>2</sup> The nanotubes can be open-ended or closed by caps containing five-membered rings. They can be multi- (MWNTs) or single-walled (SWNTs). We show a typical high-resolution electron

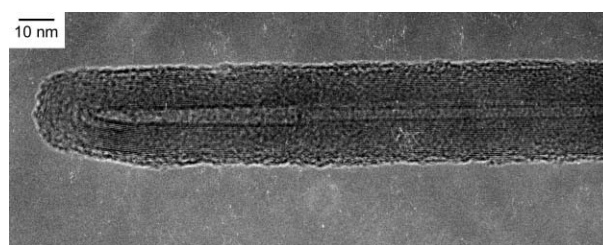


Fig. 1 A typical TEM image of a closed, multi-walled carbon nanotube. The separation between the graphite layers is 0.34 nm.

microscope (HREM) image of a multi-walled nanotube in Fig. 1. Depending on the way the graphene sheets fold, nanotubes are classified as armchair, zigzag or chiral as shown in Fig. 2. The electrical conductivity of the nanotubes depends on the nature of folding.

Several layered inorganic compounds possess structures comparable to the structure of graphite, the metal dichalcogenides being important examples. The metal dichalcogenides, MX<sub>2</sub> (M = Mo, W, Nb, Hf; X = S, Se) contain a metal layer sandwiched between two chalcogen layers with the metal in a trigonal pyramidal or octahedral coordination mode.<sup>3</sup> The MX<sub>2</sub> layers are stacked along the *c*-direction in ABAB fashion. The MX<sub>2</sub> layers are analogous to the single graphene sheets in the graphite structure (Fig. 3). When viewed parallel to the *c*-axis, the layers show the presence of dangling bonds due to the absence of an X or M atom at the edges. Such unsaturated bonds at the edges of the layers also occur in graphite. The dichalcogenide layers are unstable towards bending and have a high propensity to roll into curved structures. Folding in the

† The illustration of John Dalton (reproduced courtesy of the Library and Information Centre, Royal Society of Chemistry) marks the 200th anniversary of his investigations which led to the determination of atomic weights for hydrogen, nitrogen, carbon, oxygen, phosphorus and sulfur.

C. N. R. Rao was born in Bangalore, India in 1934. He received his MSc degree from the Banaras Hindu University, PhD from Purdue University and DSc from the University of Mysore. Following postdoctoral work at the University of California, Berkeley, he joined the faculty at the Indian Institute of Science, Bangalore. He later moved to the Indian Institute of Technology, Kanpur where he was Professor and Head of the Department of Chemistry. He returned to the Indian Institute of Science, Bangalore in 1976 to start a new



C. N. R. Rao

unit devoted to Solid State and Structural Chemistry. He also founded the Jawaharlal Nehru Centre for Advanced Scientific Research, Bangalore in 1989. His main research interests are in solid state and materials chemistry. He is a Fellow of the Royal Society, London, and is a member of a several other academies. He is an honorary fellow of the Royal Society of Chemistry and is the recipient of the Hughes Medal of the Royal Society.

Manashi Nath was born in Calcutta in 1976 and received her BSc degree from the Presidency College, Calcutta in 1997. She is a student of the integrated PhD programme of the Indian Institute of Science, Bangalore and received her MSc degree in 2000. She has worked mainly on inorganic nanotubes.



Manashi Nath

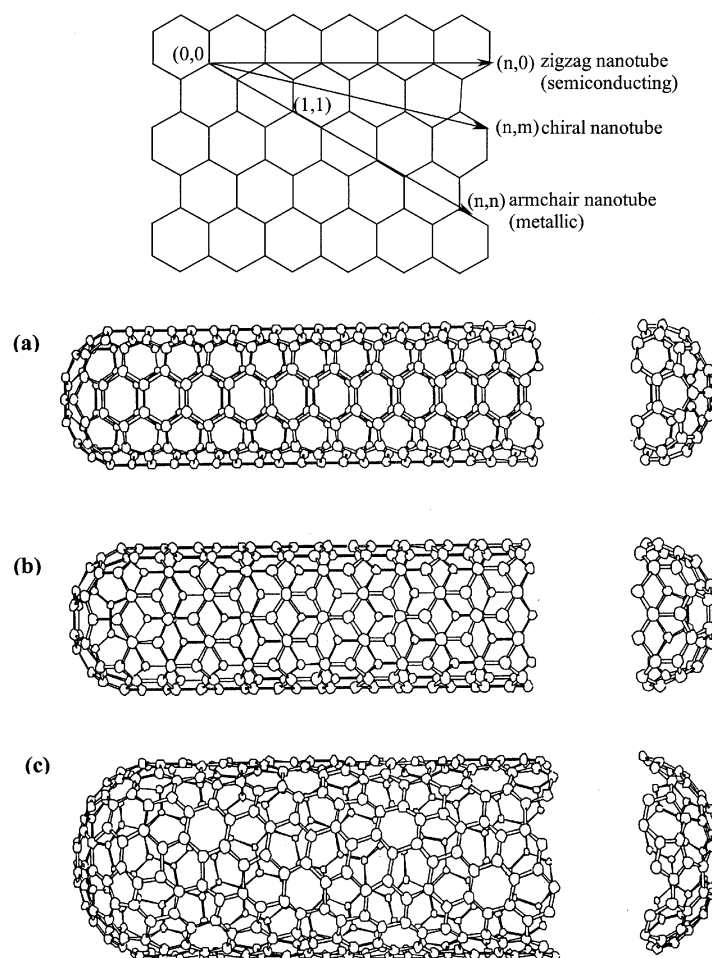


**Fig. 2** Schematic representation of the folding of a graphene sheet into (a) zigzag, (b) armchair and (c) chiral nanotubes.

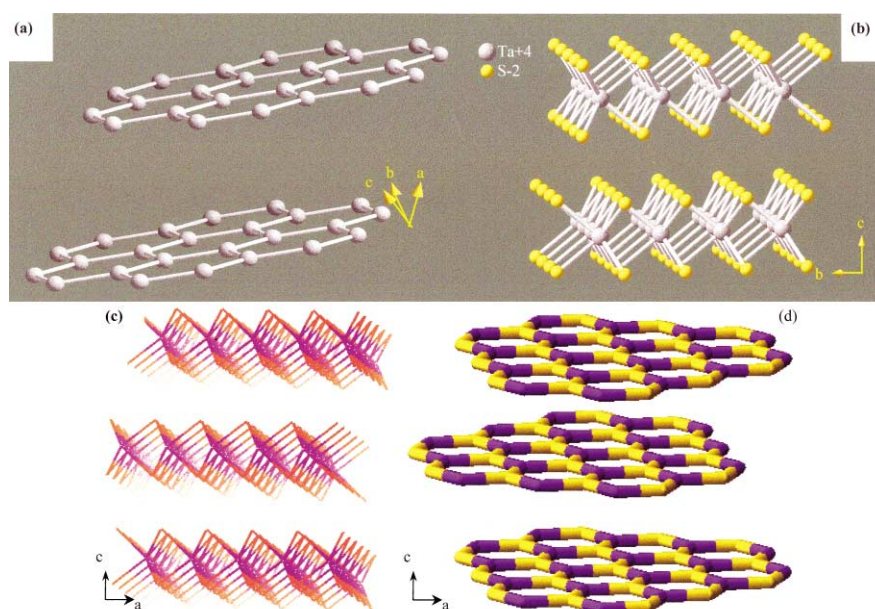


**Fig. 3** Comparison of the structures of (a) graphite and inorganic layered compounds such as (b) NbS<sub>2</sub>/TaS<sub>2</sub>; (c) MoS<sub>2</sub>; (d) BN. In the layered dichalcogenides, the metal is in trigonal prismatic (TaS<sub>2</sub>) or octahedral coordination (MoS<sub>2</sub>).

layered transition metal chalcogenides (LTMCS) was recognized as early as 1979, well before the discovery of the carbon nanotubes. Rag-like and tubular structures of MoS<sub>2</sub> were reported by Chianelli<sup>4</sup> who studied their usefulness in catalysis.

The folded sheets appear as crystalline needles in low magnification transmission electron microscope (TEM) images, and were described as layers that fold onto themselves (Fig. 4). These

structures indeed represent those of nanotubes. Tenne *et al.*<sup>5</sup> first demonstrated that Mo and W dichalcogenides are capable of forming nanotubes (Fig. 5a). Closed fullerene-type structures (*inorganic fullerenes*) also formed along with the nanotubes (Fig. 5b). The dichalcogenide structures contain concentrically nested fullerene cylinders, with a less regular structure than in the carbon nanotubes. Accordingly, MX<sub>2</sub> nanotubes have



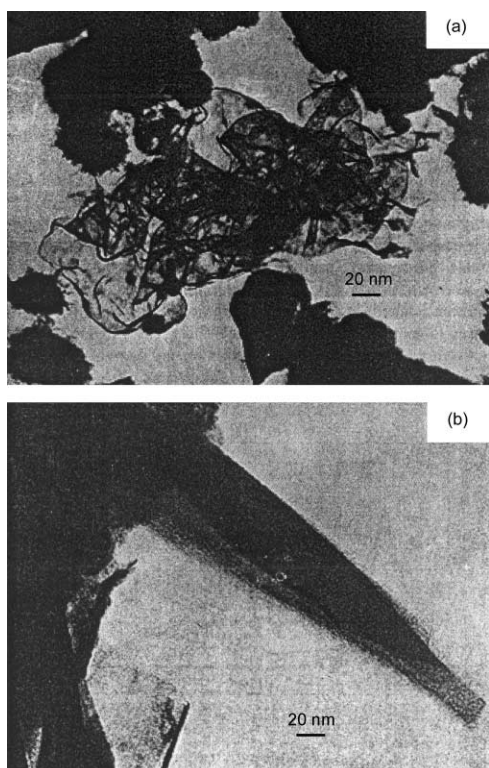


**Fig. 4** Low-magnification TEM images of (a) highly folded  $\text{MoS}_2$  needles and (b) a rolled sheet of  $\text{MoS}_2$  folded back on itself. (Reproduced with permission from ref. 4).

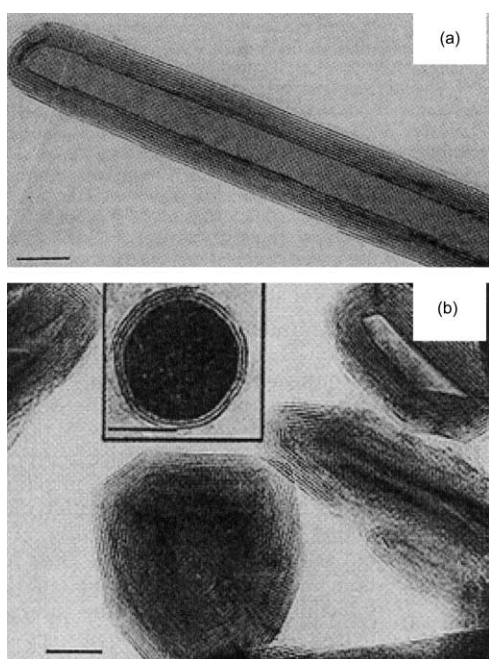


**Fig. 5** TEM images of (a) a multi-walled nanotube of  $\text{WS}_2$  and (b) hollow particles (inorganic fullerenes) of  $\text{WS}_2$ . (Reproduced with permission from refs. 5a and b, respectively).

varying wall thickness and contain some amorphous material on the exterior of the tubes. Nearly defect-free  $\text{MX}_2$  nanotubes are rigid as a consequence of their structure and do not permit plastic deformation. The folding of a  $\text{MS}_2$  layer in the process of forming a nanotube is shown in the schematic in Fig. 6. Considerable progress has been made in the synthesis of the nanotubes of Mo and W dichalcogenides in the last few years (Table 1). There has been some speculation on the cause of folding and curvature in the LTMCS. Stoichiometric LTMCS chains and layers such as those of  $\text{TiS}_2$  possess an inherent ability to bend and fold, as observed in intercalation reactions.

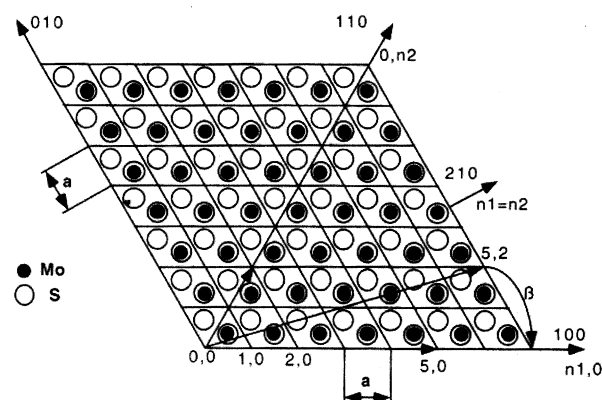


**Fig. 6** Schematic illustration of the bending of a  $\text{MoS}_2$  layer. (Reproduced with permission from ref. 19).

The existence of alternate coordination and therefore of stoichiometry in the LTMCS may also cause folding. Lastly, a change in the stoichiometry within the material would give rise to closed rings.

Transition metal chalcogenides possess a wide range of interesting physical properties. They are widely used in catalysis and as lubricants. They have both semiconducting and superconducting properties. With the synthesis and characterization of the fullerenes and nanotubes of  $\text{MoS}_2$  and  $\text{WS}_2$ , a wide field of research has opened up enabling the successful synthesis of nanotubes of other metal chalcogenides. It may be recalled that the dichalcogenides of many of the Group 4 and 5 metals have layered structures suitable for forming nanotubes.

Curved structures are not only limited to carbon and the dichalcogenides of Mo and W. Perhaps the most well-known example of a tube-like structure with diameters in the nm range is formed by the asbestos mineral (*chrysotil*) whose fibrous characteristics are determined by the tubular structure of the fused tetrahedral and octahedral layers. The synthesis of mesoporous silica with well-defined pores in the 2–20 nm range was reported by Beck and Kresge.<sup>6</sup> The synthetic strategy involved the self-assembly of liquid crystalline templates. The pore size in zeolitic and other inorganic porous solids is varied by a suitable choice of the template. However, in contrast to the synthesis of porous compounds, the synthesis of nanotubes is somewhat more difficult.

Nanotubes of oxides of several transition metals as well as of other metals have been synthesized employing different methodologies.<sup>7–12</sup> Silica nanotubes were first produced as a spin-off product during the synthesis of spherical silica particles by the hydrolysis of tetraethylorthosilicate (TEOS) in a mixture of water, ammonia, ethanol and D,L-tartaric acid.<sup>8</sup> Since self-assembly reactions are not straightforward with respect to the desired product, particularly its morphology, templated reactions have been employed using carbon nanotubes to obtain nanotube structures of metal oxides.<sup>9,10</sup> Oxides such as  $\text{V}_2\text{O}_5$  have good catalytic activity in the bulk phase. Redox catalytic activity is also retained in the nanotubular structure. There have been efforts to prepare  $\text{V}_2\text{O}_5$  nanotubes by chemical methods as well.<sup>11</sup>

Boron nitride (BN) crystallizes in a graphite-like structure and can be simply viewed as replacing a C–C pair in the graphene sheet with the iso-electronic B–N pair. It can, therefore, be considered as an ideal precursor for the formation of BN nanotubes. Replacement of the C–C pairs partly or entirely by the B–N pairs in the hexagonal network of graphite leads to the formation of a wide array of two-dimensional phases that can form hollow cage structures and nanotubes. The possibility of replacing C–C pairs by B–N pairs in the hollow cage structure of  $\text{C}_{60}$  was predicted<sup>13</sup> and verified experimentally.<sup>14</sup> BN-doped carbon nanotubes have been prepared.<sup>15</sup> Pure BN nanotubes have been generated by employing several

Table 1 Synthetic strategies for various chalcogenide nanotubes

Chalcogenide	Synthetic strategy	Ref.	Chalcogenide	Synthetic strategy	Ref.
WS <sub>2</sub>	(i) Heating MoO <sub>3</sub> in the presence of forming gas followed by heating in H <sub>2</sub> S	5a	Mo <sub>x</sub> W <sub>y</sub> C <sub>z</sub> S <sub>2</sub>	Pyrolysis of H <sub>2</sub> S over carbon-containing W and Mo-oxide complexes	43
	(ii) WS <sub>3</sub> and (NH <sub>4</sub> ) <sub>2</sub> WSe <sub>4</sub> decomposition in H <sub>2</sub>	21	Nb–W–S	Heating Nb <sub>2</sub> O <sub>5</sub> coated W <sub>18</sub> O <sub>49</sub> nanorods in H <sub>2</sub> S at 1100 °C	41
	(iii) Pyrolysis of H <sub>2</sub> S/N <sub>2</sub> over WO <sub>3</sub> -coated MWNTs	45a,b			
	(iv) Laser ablation of WS <sub>2</sub> target	64			
MoS <sub>2</sub>	(i) Heating MoO <sub>3</sub> in the presence of forming gas followed by heating in H <sub>2</sub> S	5b,c	Mo–Ti–S	Pyrolysis of H <sub>2</sub> S/N <sub>2</sub> mixture over Ti–Mo alloy at elevated temperatures	42
	(ii) Decomposition of (NH <sub>4</sub> ) <sub>2</sub> MoS <sub>4</sub> in the pores of anodic alumina	31	NbS <sub>2</sub>	(i) NbS <sub>3</sub> decomposition	23
	(iii) Decomposition of (NH <sub>4</sub> ) <sub>2</sub> MoS <sub>4</sub> MoS <sub>3</sub> in H <sub>2</sub>	21		(ii) CNT templated reaction	46
	(iv) Hydrothermal treatment of ammonium thiomolybdate with ethylenediamine	62	TaS <sub>2</sub>	TaS <sub>3</sub> decomposition	23
	(v) MoS <sub>2</sub> powder covered with Mo foil, heated to 1300 °C in H <sub>2</sub> S	61	HfS <sub>2</sub> ZrS <sub>2</sub>	Decomposition of HfS <sub>3</sub>	24
	(vi) Laser ablation of MoS <sub>2</sub> target	64		Decomposition of ZrS <sub>3</sub>	24
MoS <sub>2</sub> I <sub>x</sub>	MoS <sub>2</sub> with I <sub>2</sub> and C <sub>60</sub> as carrier	63	NbSe <sub>2</sub>	(i) NbSe <sub>3</sub> decomposition	70
MoSe <sub>2</sub>	(i) MoO <sub>3</sub> + H <sub>2</sub> Se	20a	CdS, CdSe	(ii) Electron irradiation of NbSe <sub>2</sub>	69
	(ii) MoSe <sub>3</sub> and (NH <sub>4</sub> ) <sub>2</sub> MoSe <sub>4</sub> decomposition in H <sub>2</sub>	22		Surfactant-assisted synthesis	28,75
WSe <sub>2</sub>			ZnS	Sulfidization of ZnO columns by H <sub>2</sub> S at 400 followed by etching the core	77
	(i) WO <sub>3</sub> + Se vapors at 650–850 °C	20a	NiS	Treatment of Ni(NH <sub>3</sub> ) <sub>4</sub> <sup>2+</sup> complex with CS <sub>2</sub> in aqueous ammonia	78
	(ii) Electron irradiation of WSe <sub>2</sub>	20b		Hydrothermal reaction between Cu and S in presence of LiOH.H <sub>2</sub> O and trace amount of Fe	79

procedures, yielding nanotubes with varying wall thickness and morphology.<sup>16,17</sup> It is therefore quite possible that nanotube structures of other layered materials can be prepared as well. For example, many metal halides (*e.g.*,  $\text{NiCl}_2$ ), oxides ( $\text{GeO}_2$ ) and nitrides ( $\text{GaN}$ ) crystallize in layered structures. There is considerable interest at present to prepare exotic nanotubes and to study their properties.

In this article, we discuss the synthesis and characterization of nanotubes of chalcogenides of Mo, W and other metals, metal oxides, BN and other materials and present the current status of the subject. We briefly examine some of the important properties of the inorganic nanotubes and indicate possible future directions.

## 2. General synthetic strategies

Several strategies have been employed for the synthesis of carbon nanotubes.<sup>2</sup> They are generally made by the arc evaporation of graphite or by the pyrolysis of hydrocarbons such as acetylene or benzene over metal nanoparticles in a reducing atmosphere. Pyrolysis of organometallic precursors provides a one-step synthetic method of making carbon nanotubes.<sup>18</sup> In addition to the above methods, carbon nanotubes have been prepared by laser ablation of graphite or electron-beam evaporation. Electrochemical synthesis of nanotubes as well as growth inside the pores of alumina membranes have also been reported. The above methods broadly fall under two categories. Methods such as the arc evaporation of graphite employ processes which are far from equilibrium. The chemical routes are generally closer to equilibrium conditions. Nanotubes of metal chalcogenides and boron nitride are also prepared by employing techniques similar to those of carbon nanotubes, although there is an inherent difference in that the nanotubes of inorganic materials such as  $\text{MoS}_2$  or BN would require reactions involving the component elements or compounds containing the elements. Decomposition of precursor compounds containing the elements is another possible route.

Nanotubes of dichalcogenides such as  $\text{MoS}_2$ ,  $\text{MoSe}_2$  and  $\text{WS}_2$  are also obtained by employing processes far from equilibrium such as arc discharge and laser ablation.<sup>19</sup> By far the most successful routes employ appropriate chemical reactions. Thus,  $\text{MoS}_2$  and  $\text{WS}_2$  nanotubes are conveniently prepared starting with the stable oxides,  $\text{MoO}_3$  and  $\text{WO}_3$ .<sup>5</sup> The oxides are first heated at high temperatures in a reducing atmosphere and then reacted with  $\text{H}_2\text{S}$ . Reaction with  $\text{H}_2\text{Se}$  is used to obtain the selenides.<sup>20</sup> Recognizing that the trisulfides  $\text{MoS}_3$  and  $\text{WS}_3$  are likely to be the intermediates in the formation of the disulfide nanotubes, the trisulfides have been directly decomposed to obtain the disulfide nanotubes.<sup>21</sup> Diselenide nanotubes have been obtained from the metal triselenides.<sup>22</sup> The trisulfide route is indeed found to provide a general route for the synthesis of the nanotubes of many metal disulfides such as  $\text{NbS}_2$ <sup>23</sup> and  $\text{HfS}_2$ .<sup>24</sup> In the case of Mo and W dichalcogenides, it is possible to use the decomposition of the precursor ammonium salt, such as  $(\text{NH}_4)_2\text{MX}_4$  ( $\text{X} = \text{S}, \text{Se}; \text{M} = \text{Mo}, \text{W}$ ) as a means of preparing the nanotubes.<sup>21</sup> Other methods employed for the synthesis of dichalcogenide nanotubes include hydrothermal methods where the organic amine is taken as one of the components in the reaction mixture (Table 1).

The hydrothermal route has been used for synthesizing nanotubes and related structures of a variety of other inorganic materials as well. Thus, nanotubes of several metal oxides (*e.g.*,  $\text{SiO}_2$ ,<sup>25</sup>  $\text{V}_2\text{O}_5$ ,<sup>11</sup>  $\text{ZnO}$ <sup>26</sup>) have been produced hydrothermally. Nanotubes of oxides such as  $\text{V}_2\text{O}_5$  are also conveniently prepared from a suitable metal oxide precursor in the presence of an organic amine or a surfactant.<sup>27</sup> Surfactant-assisted synthesis of CdSe and CdS nanotubes has been reported. Here the metal oxide reacts with the sulfidizing/selenidizing agent in the presence of a surfactant such as TritonX.<sup>28</sup>

Sol-gel chemistry is widely used in the synthesis of metal

oxide nanotubes, a good example being that of silica<sup>8</sup> and  $\text{TiO}_2$ .<sup>29</sup> Oxide gels in the presence of surfactants or suitable templates form nanotubes. For example, by coating carbon nanotubes (CNTs) with oxide gels and then burning off the carbon, one obtains nanotubes and nanowires of a variety of metal oxides including  $\text{ZrO}_2$ ,  $\text{SiO}_2$  and  $\text{MoO}_3$ .<sup>10,30</sup> Sol-gel synthesis of oxide nanotubes is also possible in the pores of alumina membranes. It should be noted that  $\text{MoS}_2$  nanotubes are also prepared by the decomposition of a precursor in the pores of an alumina membrane.<sup>31</sup>

Boron nitride nanotubes have been obtained by striking an electric arc between  $\text{HfB}_2$  electrodes in a  $\text{N}_2$  atmosphere.<sup>32</sup> BCN and BC nanotubes are obtained by arcing between B/C electrodes in an appropriate atmosphere. A greater effort has gone into the synthesis of BN nanotubes starting with different precursor molecules containing B and N. Decomposition of borazine in the presence of transition metal nanoparticles and the decomposition of the 1 : 2 melamine-boric acid addition compound yield BN nanotubes.<sup>16</sup> Reaction of boric acid or  $\text{B}_2\text{O}_3$  with  $\text{N}_2$  or  $\text{NH}_3$  at high temperature in the presence of activated carbon, carbon nanotubes or catalytic metal particles has been employed to synthesize BN nanotubes.<sup>17</sup>

## 3. Nanotubes of Mo and W dichalcogenides

Nanotubes of the disulfides and diselenides of Mo and W have been prepared by employing several strategies. The first synthesis of the  $\text{MoS}_2$  and  $\text{WS}_2$  nanotubes was carried out by Tenne *et al.*<sup>5</sup> by treating the metal oxides in an atmosphere of forming gas (95%  $\text{N}_2$  + 5%  $\text{H}_2$ ), followed by heating in a stream of  $\text{H}_2\text{S}$  at elevated temperatures. Initially, the oxides are reduced to the suboxides which are then converted to the sulfides. Onion-like structures analogous to nested fullerenes were also obtained in considerable yields (Fig. 5). The heating arrangement with a tubular furnace employed for the preparation of  $\text{MoS}_2$  nanotubes is shown in Fig. 7.  $\text{MoO}_3$  being sublimable, the

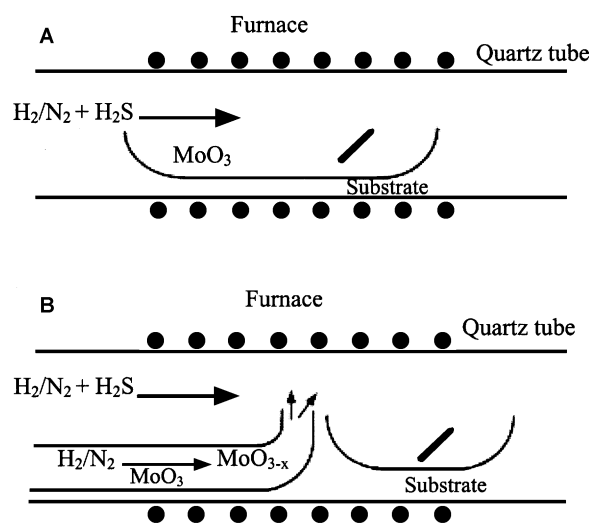


**Fig. 7** (A) Schematic of the gas-phase reactor used to produce  $\text{MoS}_2$  nanotubes; (B) a modification of the above where molybdenum suboxide flow was introduced through a separate tube and the collecting substrate was placed behind a high wall. (Reproduced with permission from ref. 5c).

growth of  $\text{MoS}_2$  occurred from the vapor phase. On the other hand  $\text{WO}_{3-x}$ , not being volatile, the growth of  $\text{WS}_2$  took place at the vapor-solid interface. Following the initial synthesis, various modifications have been adopted. Instead of starting with oxide particles, preformed morphologies like needles and whiskers containing the desired shapes of the nanotube products were also used as precursors. Thus, thermal treatment of the oxide needles in  $\text{H}_2\text{S}$  gave  $\text{WS}_2$  nanotubes.<sup>19</sup> In these pro-



cesses, the metal trisulfide is first formed on heating the oxide in an excess of  $\text{H}_2\text{S}$ . The trisulfide loses sulfur on annealing and crystallizes in the form of a disulfide nanoparticle or nanotube.  $\text{MoS}_2$  nanotubes have also been prepared from the  $\text{MoS}_3$  by sending a pulse through a STM tip.<sup>33</sup> The tip induced the crystallization of amorphous  $\text{MoS}_3$  films deposited on a gold substrate producing inorganic fullerenes, some of them containing  $\text{MoS}_3$  in the core, while the rest are hollow nanoparticles (Fig. 8).

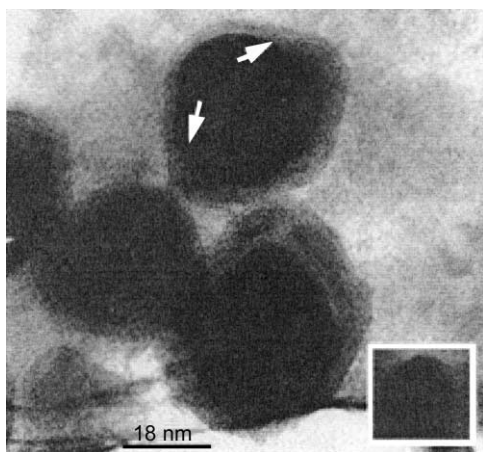
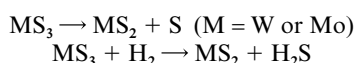


**Fig. 8** Crystalline IF- $\text{MoS}_2$  nanoparticles with a  $\text{MoS}_3$  core. Inset shows a fullerene-like nanoparticle of  $\sim 15$  nm diameter. (Reproduced with permission from ref. 33).

On heating the nanorods or needles of the precursor oxide particles in an atmosphere of flowing  $\text{H}_2\text{S}$  or  $\text{H}_2\text{Se}$ , the outermost oxide layers are first converted to the chalcogenide layers. Further agglomeration of the oxidic particles is inhibited by the inert layer coating. Fast diffusion of  $\text{H}_2$  into the precursor nanoparticle leads to the reduction of the core to the suboxide form. The second stage of the reaction involves the slow diffusion of the sulfur vapor into the core and the conversion of the oxide core to the sulfide. This mechanism has been substantiated by the presence of an incompletely sulfidized oxide core or even the metal in some of the  $\text{WS}_2$  nanotubes.<sup>34,35</sup> The growth mechanism of the disulfide nanotubes from the suboxide particles comprises several steps. In the first step, the oxide particles react with  $\text{H}_2\text{S}$  to form one or two layers of the sulfide. This prevents further aggregation of the precursor particles and the formation of larger particles. Diffusion of  $\text{H}_2$  into the particle and the out-diffusion of  $\text{O}_2$  leads to the reduction of the oxide particles and the creation of crystallographic shear planes. In the next step of the reaction, sulfur vapor diffuses slowly into the precursor particles converting the suboxide core to the sulfide, which becomes hollow at the end of the process. The growth front is near the core of the precursor particle.

The knowledge that  $\text{MoS}_3$  and  $\text{WS}_3$  are the stable phases at low temperatures in the excess sulfur regime,<sup>36</sup> and that these amorphous trisulfides are first formed when the metal trioxide reacts with  $\text{H}_2\text{S}$ ,<sup>37</sup> underscores the role of the trisulfide as a likely intermediate in the formation of the disulfide. A study of the binary metal-sulfur (Mo(W)-S) phase diagram reveals that the inorganic fullerene phase is obtained at the phase boundary between the amorphous  $\text{MS}_3$  and the crystalline  $\text{MS}_2$  phases. The loss of sulfur from the  $\text{MS}_3$  phase triggers the nucleation of the  $\text{MS}_2$  nanoparticles. By starting with a trisulfide, it should therefore be possible to obtain the disulfide nanostructure by thermal decomposition or by reacting with hydrogen.<sup>38,39</sup>



Thermal decomposition of amorphous Mo and W trisulfides has been investigated under a steady gas flow, to explore the

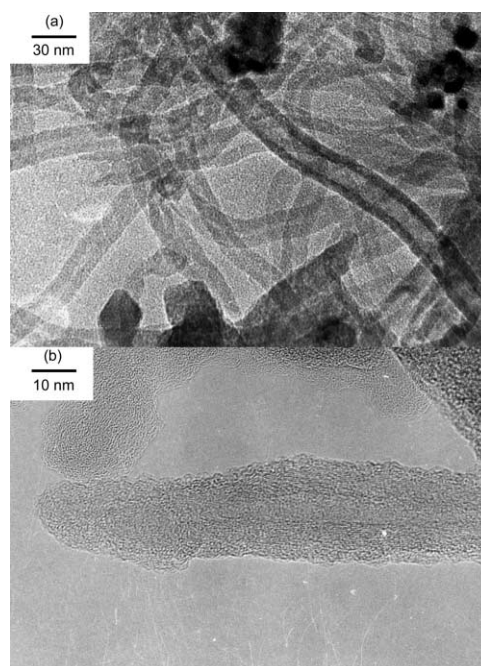


**Fig. 9** TEM images of  $\text{MoS}_2$  nanotubes grown by the decomposition of  $\text{MoS}_3$ . (Reproduced with permission from ref. 21).

formation of the disulfide nanotubes under a steady flow of hydrogen (100 sccm).<sup>21</sup> The decomposition products consisted of a high proportion of disulfide nanotubes (Fig. 9).

Mo and W trisulfides themselves are prepared by thermal decomposition of the ammonium thiometallates,  $(\text{NH}_4)_2\text{MS}_4$  ( $\text{M} = \text{Mo, W}$ ).<sup>38</sup> Accordingly, direct decomposition of the ammonium thiometallates in  $\text{H}_2$  yields the  $\text{MoS}_2$  and  $\text{WS}_2$  nanotubes (Fig. 10).<sup>21</sup> In addition to providing a direct method

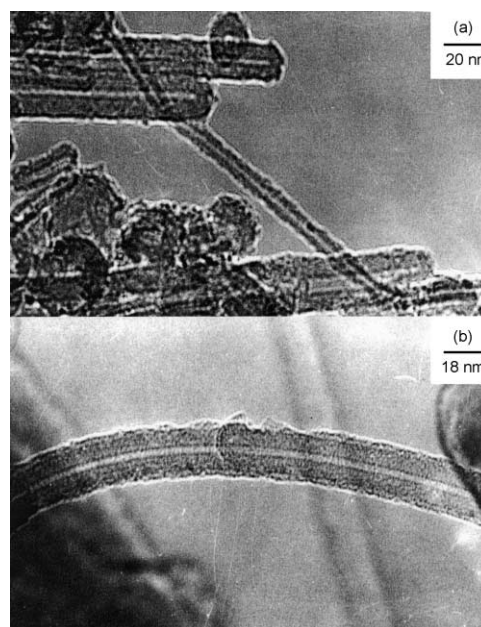
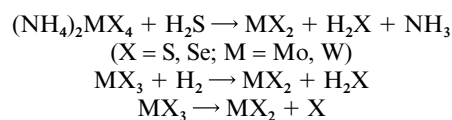


**Fig. 10** (a) Low-resolution TEM images of  $\text{MoS}_2$  nanotubes grown by the decomposition of ammonium thiomolybdate; (b) HREM image of the  $\text{MoS}_2$  nanotube. (Reproduced with permission from ref. 21).

for the preparation of dichalcogenide nanotubes,<sup>21</sup> the trichalcogenide or the ammonium chalcometallate route enables the easy synthesis of nanotubes of the other layered dichalcogenides as well.<sup>22-24</sup>



Thus, nanotubes of Mo and W diselenides have been prepared by the decomposition of the triselenide or the ammonium selenometallate at elevated temperatures under a flow of  $H_2$ .<sup>22</sup> Apart from the nanotubes, nanorods of  $WSe_2$  were also obtained. Some of the nanorods were attached to an amorphous particle at the tip (Fig. 11a). Several single-walled  $WSe_2$

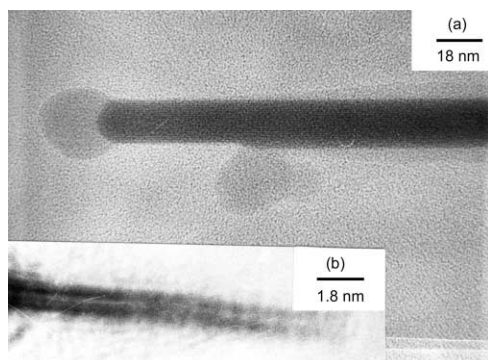


**Fig. 11** (a) TEM image of a  $WSe_2$  nanorod with a particle attached at the tip, grown by the decomposition of  $WSe_3$ ; (b) single-walled  $WSe_2$  nanorod. (Reproduced with permission from ref. 22).

nanotubes were also observed (Fig. 11b). This strategy has been employed to obtain W doped  $MoS_2$  nanotubes.<sup>40</sup> Thus, solid solutions of the ammonium thiometallates,  $(NH_4)_2Mo_{1-x}W_xS_4$  with varying ratios of Mo : W were used as precursors, to yield  $Mo_{1-x}W_xS_2$  nanotubes ( $x = 0.15-0.5$ ) on thermal decomposition under a gas flow ( $H_2$ , He or Ar) at  $\sim 770^\circ C$  (Fig. 12).

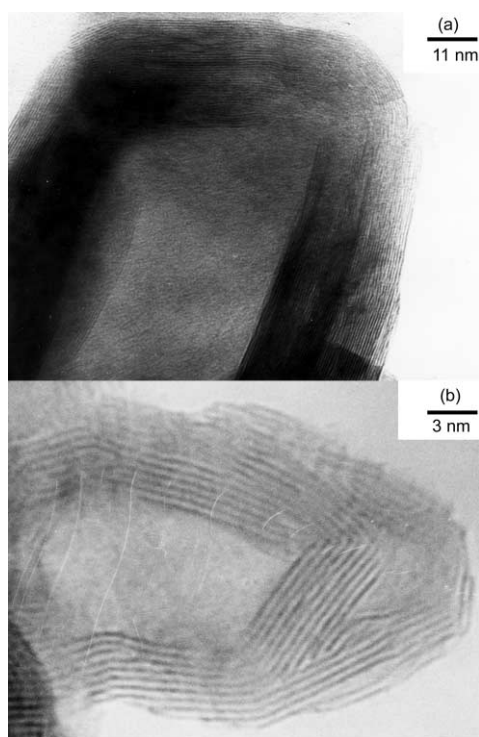


**Fig. 12** HREM image of  $Mo_{1-x}W_xS_2$  nanotubes showing a rectangular tip in (a) and (b) bamboo-like stacking. The layer separation in the walls is  $\sim 0.62$  nm. (Reproduced with permission from ref. 40).

SWNTs of the doped sulfide structures were also observed. In general, the yield of nanotubes decreased with the increase in W content in the host  $MoS_2$  lattice. Increasing the W content in  $MoS_2$  also increases the layer mismatch in the tube walls and defects.

Other metals have been doped in the host disulfide layers of the nanotubes by using methodologies similar to those employed for the parent disulfides. Thus, composite nanotubes

of  $W-Nb-S$ ,<sup>41</sup>  $Ti-Mo-S$ <sup>42</sup> and  $Mo-W-C-S$ <sup>43</sup> have been prepared where the precursor was a mixed oxide of the two metals. In the case of  $Ti-Mo-S$ , the  $Ti-Mo$  alloy heated in oxygen to yield the mixed oxide, which was further heated in forming gas followed by  $H_2S$  to produce  $Ti$  doped  $MoS_2$  nanotubes (Fig. 13).

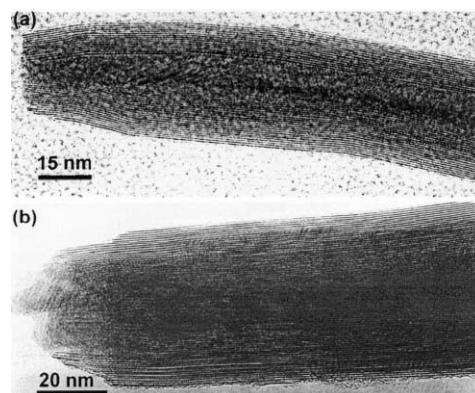


**Fig. 13** TEM images of hollow  $Ti-Mo-S$  nanotubes. (Reproduced with permission from ref. 42).

The  $W-Nb$  mixed metal oxide was prepared by sonicating the solution containing the precursors. Treatment of the mixed metal oxide precursors in  $H_2S$  produced the Nb doped  $WS_2$  nanotubes (Fig. 14). The mechanism of formation of the com-

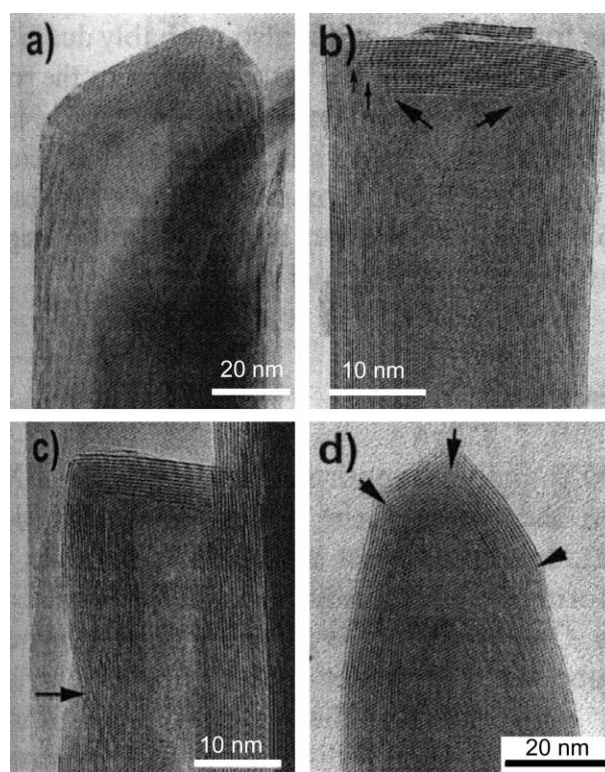


**Fig. 14** HREM images of  $Nb-W-S$  nanotubes showing various tube closures: (a) an irregular tube closure; (b) a  $90^\circ$  wall-tip junction; (c) another near  $90^\circ$  closure (the arrow points to the buckling defect in the tube wall); (d) an irregular closure with severe bending defects. (Reproduced with permission from ref. 41).

posite nanotubes is similar to that of the binary nanotubes of  $MoS_2$  and  $WS_2$  and involves a layer by layer conversion of the mixed metal oxide to the sulfide. Some of the layers in the nanotube walls terminate abruptly, probably because of the exhaustion of the growing materials at that edge. The metal particles present at the terminated edge also inhibit the growth,<sup>44</sup> as in the case of metal oxide promoted growth of the BN nanotubes.



The methods of preparation discussed above do not involve any template, and the nanoparticles of the oxide or the trisulfide act as nucleation centers for tube growth. Recently, CNTs have been used as templates to grow  $\text{MoS}_2$ ,  $\text{WS}_2$  and  $\text{NbS}_2$  coated carbon nanotubes, some of which contain 1–2 layers of the chalcogenide at the exterior.<sup>45,46</sup> The CNTs were coated with the metal oxide or its precursor and treated in a  $\text{H}_2\text{S}/\text{H}_2/\text{N}_2$  atmosphere at elevated temperatures to convert the oxide to the sulfide. However, the CNT core was not removed in the nanostructures (Fig. 15).

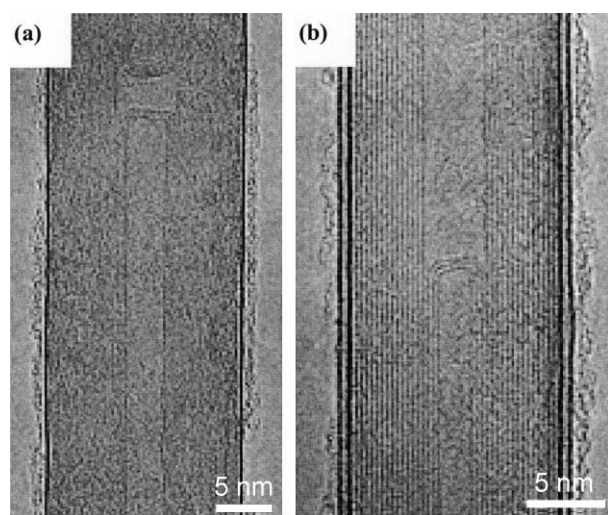


**Fig. 15** HREM image of a CNT coated with (a) a single layer and (b) a double layer of  $\text{WS}_2$ . (Reproduced with permission from ref. 45a).

Confined reactions have been used to control the size of  $\text{MoS}_2$  nanotubes. For example,  $\text{MoS}_2$  nanotubes have been grown in the voids of an anodic alumina membrane, by decomposing  $(\text{NH}_4)_2\text{MoS}_4$  inside the pores of the membrane.<sup>31</sup> The membrane is dissolved by treatment with alkali to yield free tubes. This method yields large diameter  $\text{MoS}_2$  nanotubes.

As mentioned earlier, the structure of  $\text{MoS}_2$  consists of the disulfide layers stacked along the  $c$ -direction.<sup>3</sup> This implies that the S–S interaction between the  $\text{MoS}_2$  slabs is weaker compared to the intralayer interactions. The S–S interlayer distances are therefore susceptible to distortions during the folding of the layers. This is exemplified by the slight expansion of the  $c$ -axis (2%) in the  $\text{MoS}_2$  nanotubes.<sup>19</sup> High resolution (HREM) images of the disulfide nanotubes show stacking of the (002) planes parallel to the tube axis. The distance between the layer fringes corresponds to the  $d(002)$  spacing.

Nanotubes of the disulfides are open-ended or capped. However, the closed end of the nanotube is not exactly spherical. Polygonal caps and rectangular tips are frequently observed in the disulfide nanotubes<sup>47</sup> (Fig. 16). Various types of open ends of nanotubes have been observed. They include flat open ends, conical open ends and also open-ended tubes where the layers at the tip arrange in peculiar ways giving the appearance of a pseudo closed tip.<sup>47,48</sup> The outer layer of the disulfide nanotubes and inorganic fullerenes are almost always complete, but the inner layers show defects, dislocations and terminated growth. This results in differences in the wall thickness on the two sides and in the varying diameter of the inner core along the length of the tube wall. This type of terminated growth is not observed in the CNTs, but has been found in metal-filled CNTs.<sup>49</sup> The terminated layer may be a manifestation of the defective structure of the starting precursor, or can be due to the absence of growing material at the edges. Layer defects have been observed in  $\text{WS}_2$  nanotubes. They can be traced back to the crystallographic shear in the starting precursor phase.<sup>50</sup> Rémskar *et al.*<sup>51</sup> showed that each  $\text{WS}_2$  layer has to satisfy the stacking order and orientation relationship with respect to the previous layer

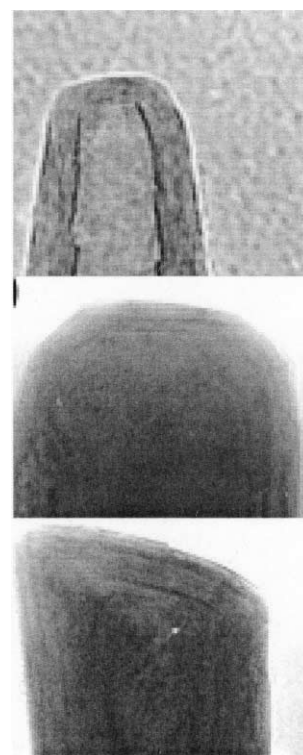


**Fig. 16** Various closed tips observed in  $\text{WS}_2$  tubes possibly containing square or octagonal defects. (Reproduced with permission from ref. 47).

and the strain involved can be relaxed by the formation of edge dislocations. The outer cylinders are subjected to less stress than the inner cylinders, and this internal stress stabilizes the inner shells, while the outer layers become easy to deform resulting in a greater number of defects near the edges.

The dichalcogenide nanotubes exhibit positive and negative curvatures similar to those in the CNTs.<sup>52</sup> In the CNTs, the curvature is believed to be due to the presence of a pentagonal ring (positive curvature) and a heptagonal ring (negative curvature) in the otherwise hexagonal network of the graphene sheet.<sup>53</sup> In the  $\text{MX}_2$  layers, the absence of a central M or X atom can give rise to triangular or rhombohedral point defects, which can cause curvature in the  $\text{MX}_2$  layers similar to those obtained in the graphene sheets (Fig. 17).<sup>5,19,54</sup> These point defects lead to topological defects and a combination of topological defects can cause tube closure.<sup>55</sup> Typical topological defects are square-like and octagonal-like defects. Based on the TEM images and electron diffraction (ED) patterns, it has been shown that a combination of these can close the armchair and zigzag tubes.<sup>55</sup> The presence of a rhombohedral point defect gives sharp edges at the corners of a rectangular inorganic fullerene. Similar point defects provide nearly 90° bends at the corners of the disulfide nanotubes<sup>47</sup> as well as the doped disulfide nanotubes (Fig. 18).<sup>41</sup> Analogous to the CNTs, the  $\text{MX}_2$  tubes exhibit the energy minimized zigzag and armchair type tube morphologies.<sup>47,56,57</sup>

In  $\text{Mo}_{1-x}\text{W}_x\text{S}_2$  nanotubes, defects in the layers, such as edge mismatch, growth termination of some of the layers and disordered layer stacking, increase with increasing tungsten doping.<sup>40</sup> Layer mismatch at the edges has also been observed in composite nanotubes such as  $\text{Nb-WS}_2$ <sup>41</sup> and  $\text{Ti-MoS}_2$ ,<sup>42</sup> due to the simultaneous growth of the disulfide layers from different points on the precursor particle. In the  $\text{Mo}_{1-x}\text{W}_x\text{S}_2$  nanotubes, W occurs in the  $\text{MoS}_2$  layers, rather than having a structure with alternate layers of  $\text{MoS}_2$  and  $\text{WS}_2$ .<sup>58</sup> The intra-layer doping of W in the  $\text{MoS}_2$  layer does not cause a major structural deformation as the lattice constants of the  $\text{MoS}_2$  and  $\text{WS}_2$  are comparable. However, a slight expansion in the  $c$ -axis occurs in composite nanotubes similar to that in the  $\text{MoS}_2$  nanotubes, due to the increased strain in curving the doped layers. With the



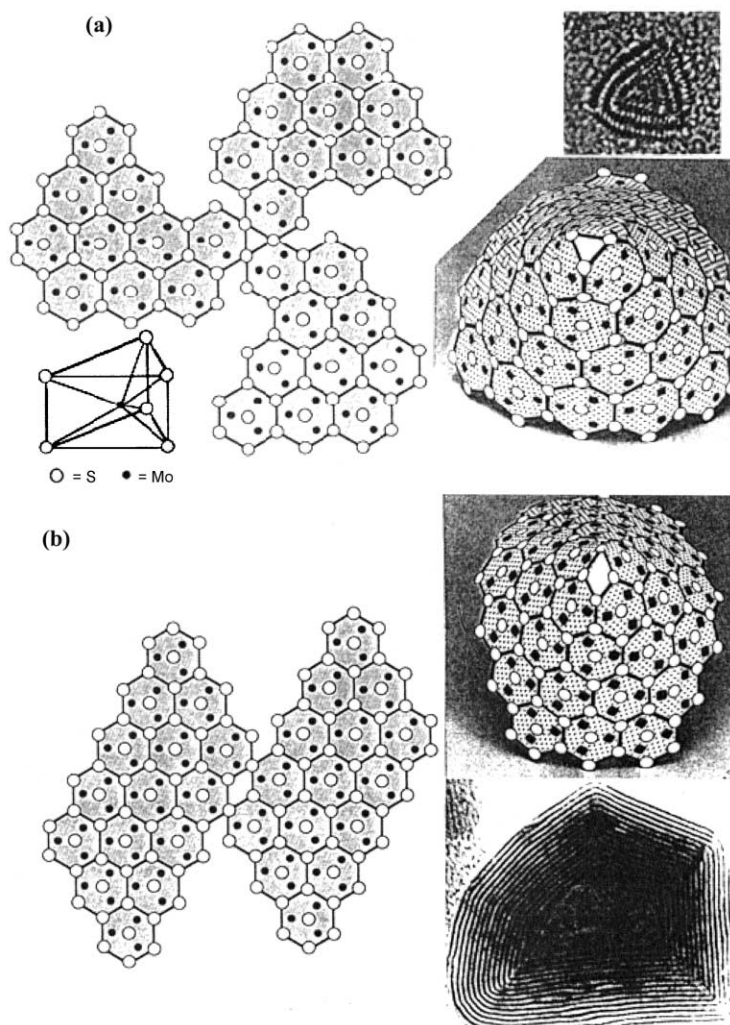


**Fig. 17** Illustration of various point defects which exists in the vertices of IF MoS<sub>2</sub>: (a) a triangular point defect; (b) a rhombohedral point defect. Insets show IF structures that are likely to contain such point defects. (Reproduced with permission from ref. 19).

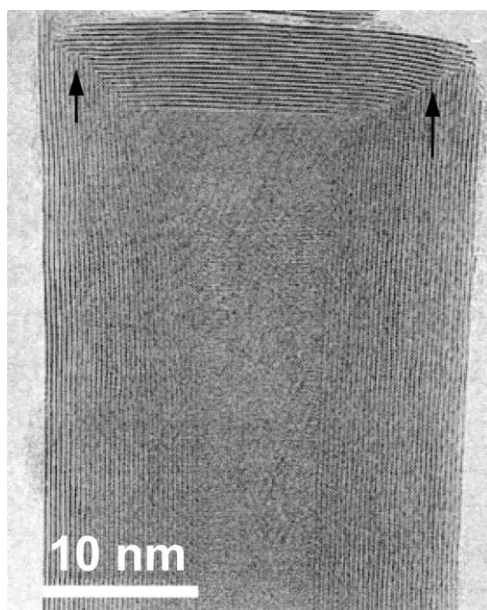


**Fig. 18** TEM image showing the sharp 90° bend observed in the W-Nb-S nanotubes. (Reproduced with permission from ref. 41a).

increasing W doping, the yield of the nanotubes decreases considerably, while other nanostructures like nanorods and nanowires are obtained in moderate yield.

Disulfide nanotubes formed from the trisulfide precursors are structurally similar to those obtained by other means. Some of

the nanotubes obtained by this method are open-ended, while others are closed. The nanotube tips are mostly non-spherical, polygonal with faceted edges. In the TEM images of MoS<sub>2</sub>, WS<sub>2</sub>, and Mo<sub>x</sub>W<sub>1-x</sub>S<sub>2</sub> nanotubes, the resolution at the tip of some of the nanotubes is lost. The ED patterns of the MoS<sub>2</sub> and WS<sub>2</sub> nanotubes prepared by this method match those reported for the armchair and zigzag tubes. It has been noticed that placing a small amount of sulfur powder near the inlet of the reaction zone, increases the yield of the nanotubes in some of the reactions. This observation suggests that the diffusion of vapors inside the particle may play a role in the formation of the nanostructures. Tenne *et al.*<sup>59</sup> have shown that the yield and diameter of the nanostructures depend on the diffusion length of the reactant vapors. In this study, MoO<sub>3</sub> was reduced to the suboxide under N<sub>2</sub> which was then carried into another reaction zone where it was converted to the sulfide. A quartz rod was used to precipitate the reaction products in order to quantify and hence study the influences of temperature, gas flow rates and diffusion rates of the reactant gases on the morphology and formation of the nanostructures.

The growth of the disulfide nanotubes from the trisulfide precursors starts with the reduction of the trisulfide precursors to a nanoparticulate form on heating in a gas flow. As the temperature reaches the decomposition temperature of the trisulfide, a few layers of the disulfide are formed at the periphery of the trisulfide particle. The growth then proceeds from “inside outwards” as the trisulfide at the core decomposes to form the disulfide layers that starts projecting outwards. This mechanism is supported by the presence of the precursor particle at the tip of some of the nanostructures, the diameter of such particles

being greater than the outer diameter of the nanostructures (Fig. 11a).<sup>22</sup> There is a simultaneous growth of the disulfide layers from different points in the precursor particle, thus resulting in a layer mismatch at the edges where the growing layers meet. In the case of  $\text{WSe}_2$ , while the nanostructures show lattice fringes with the layer separation matching that reported for the bulk, the particle at the tip appears to be due to the amorphous triselenide.

Metal-catalyzed CNT growth is diffusion-controlled, and the carbon vapor adsorbed onto the metal catalyst particles, diffuses to the rear end, from where the graphite layer grows thus encapsulating the particle inside the growing nanotubes in some cases.<sup>60</sup> The dichalcogenide tube growth is also diffusion-controlled and involves the diffusion of  $\text{H}_2\text{S}$  into the inner core of the precursor particle, which is slowly converted to the disulfide. However, in the nucleation-mediated growth of the dichalcogenide nanotubes where the trisulfide precursor acts as the nucleation center, the disulfide layer grows from the inner core of the particle and proceeds outwards.

$\text{MoS}_2$  nanotubes are also obtained by heating  $\text{MoS}_2$  powder covered with a Mo foil in the presence of  $\text{H}_2\text{S}$ .<sup>61</sup>  $\text{MoS}_2$  evaporates on heating and is deposited on the Mo foil. The hollow tubes formed exhibit a zigzag arrangement of the layers in the tube walls. In a separate hydrothermal synthesis, molybdenum polysulfide microtubules and hollow fibers were grown at room temperature from a solution containing condensed ammonium thiomolybdate and ethylene diamine. Initially, a condensed phase of the formula  $(\text{NH}_3\text{OH})_3\text{MoS}_{4.8}$  was formed. Thermal decomposition of these phases led to the formation of highly dispersed tubular  $\text{MoS}_2$ .<sup>62</sup> The amine plays an important role in nanotube formation, the absence of which yields bulk  $\text{MoS}_2$ . Ethylene diamine dihydrate appears to form chain-like structures, providing a support for formation of the nanotube. The amine is washed off to separate the hollow tubes. Bundles containing  $\text{MoS}_2\text{I}$ , single-walled nanotubes have been prepared in the presence of  $\text{C}_{60}$  as a carrier.<sup>63</sup> The presence of  $\text{C}_{60}$  was crucial in the growth process as the nanotubes failed to grow in their absence. The single-walled tubes are hexagonally packed in bundles with a cell constant of  $4.0 \text{ \AA}$  along the bundle axis and  $9.6 \text{ \AA}$  perpendicular to the axis.

Electron beam irradiation and laser ablation has been successful in producing the metal dichalcogenide nanotubes. Laser ablation of  $\text{MoS}_2$  and  $\text{WS}_2$  targets produces substantial amounts of inorganic fullerenes and nanotubes.<sup>64</sup> Electron beam irradiation of bulk  $\text{WS}_2$  powder yields various nanostructures of  $\text{WS}_2$  including inorganic fullerenes, nanotubes and nanorods.<sup>65</sup>

The disulfide nanotubes have been characterized by Raman spectroscopy. The Raman bands for the  $\text{MoS}_2$  nanotubes are similar to those of the bulk 2H-phase, except that the bands of the nanostructures show slight broadening. The composite nanotubes like those of  $\text{Ti-Mo-S}$  and  $\text{Nb-W-S}$  were also characterized by Raman spectroscopy.<sup>41,42</sup> The bands were similar to those of the undoped nanotubes, except for the appearance of a new band at  $313 \text{ cm}^{-1}$  which has been assigned to the increase in disorder owing to the presence of Nb.<sup>41</sup>

#### 4. Nanotubes of dichalcogenides of Group 4 and 5 metals

With the success in synthesising nanotubes of Mo and W dichalcogenides starting from the trichalcogenides,<sup>21,22</sup> it was realised that this methodology could prove useful to prepare the nanostructures of other metal dichalcogenides, even though the trichalcogenides may be crystalline (rather than amorphous as in the case of Mo and W), since the dichalcogenide phase appears at the boundary of the trichalcogenide phase, and the thermal decomposition of the bulk samples of the latter is known to yield dichalcogenides.<sup>39</sup>

Nath and Rao<sup>23,24</sup> have investigated the thermal decomposition of the trisulfides of Group 4 and 5 metals prepared by the conventional solid state synthesis route. The decomposition of the trisulfides of Zr, Hf, Nb and Ta in a reducing atmosphere at elevated temperatures has indeed produced good yields of nanostructures, including nanotubes and nanorods.

##### 4.1. $\text{HfS}_2$ nanotubes

Nanotubes of  $\text{HfS}_2$  are obtained by the decomposition of  $\text{HfS}_3$  in an atmosphere of  $\text{H}_2 + \text{Ar}$  (1 : 9), at 1170 K.<sup>24</sup> The product contained a good yield of the nanostructures as can be seen from the SEM image in Fig. 19a. EDX analysis revealed the

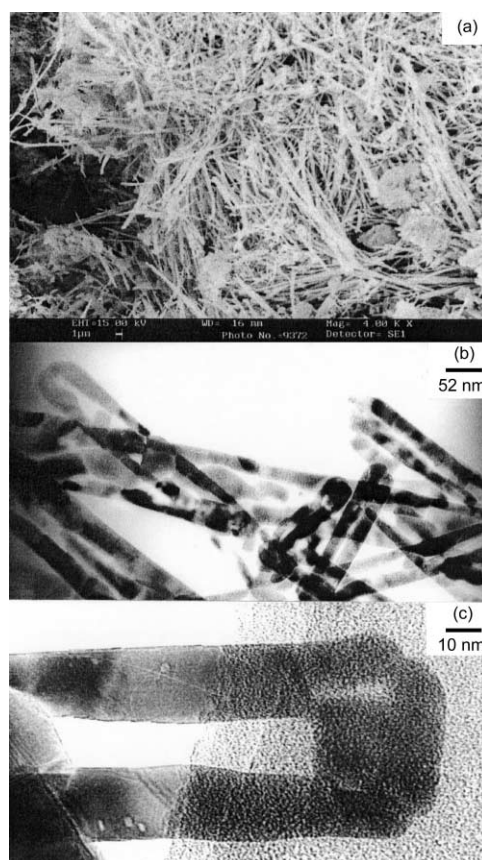


**Fig. 19** (a) SEM image of the  $\text{HfS}_2$  nanostructures; (b) and (c) low-resolution TEM images showing hollow nanotubes. The tube in (c) has a flat tip.

chemical composition to be  $\text{HfS}_2$ , while the XRD pattern showed it to be hexagonal. There is a slight expansion of the lattice in the  $c$ -direction ( $\sim 1\%$ ) of the nanotubes as compared to bulk  $\text{HfS}_2$ . The lattice expansion is less than that observed with the  $\text{MoS}_2$  and  $\text{WS}_2$  nanotubes (2–3%).<sup>19</sup> This can be attributed to the fact that the mean compressibility factor of the  $c$ -axis in  $\text{HfS}_2$  is higher than that observed for  $\text{MoS}_2$ .<sup>66</sup> The nanostructures as can be seen from the SEM image on Fig. 19a are quite lengthy, some being more than a micron long. Interestingly, a large proportion of these nanostructures are nanotubes. The low-resolution TEM image in Fig. 19b shows several nanotubes, some of which are closed with a non-spherical, nearly rectangular tip. The image in Fig. 19c shows a single nanotube with a rectangular tip, showing ripple-like undulations near the bend, which can arise from the strain involved in bending the layers. On close inspection, layer fringes are visible along the tube walls. Interrupted layer growth is observed in the inner edge of the tube wall, causing terminated layers and has non-uniformity in the wall thickness. This type of rectangular tip and terminated layer growth has also been observed in  $\text{MoS}_2$ ,  $\text{WS}_2$  and  $\text{Mo}_{1-x}\text{W}_x\text{S}_2$  nanotubes.<sup>40,47</sup>



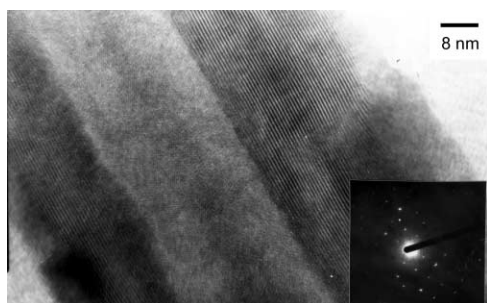


**Fig. 20** HREM image of the  $\text{HfS}_2$  nanotubes, showing a layer separation of  $\sim 0.6$  nm in the walls. Inset shows a typical ED pattern.

A high-resolution image of a  $\text{HfS}_2$  nanotube is shown in Fig. 20. The layers are separated by  $\sim 5.8$  Å corresponding to the spacing of the (001) planes. Several terminated layers are observed at the outer edge of the tube wall possibly due to the absence of the growing material at these edges. A considerable number of defects and edge dislocations are also present along the length of the tube wall. The inset in Fig. 20 shows a ED pattern of the nanotube, characteristic of the hexagonal arrangement of the layers. Bragg spots corresponding to  $d(002)$  plane (2.923 Å) are seen. The ED pattern together with the high-resolution image indicate that the growth axis of the nanotube is perpendicular to the  $c$ -direction.

Bulk  $\text{HfS}_2$  is an indirect band gap semiconductor with an indirect band gap energy of  $\sim 2.1$  eV.<sup>67</sup> The reflectance spectrum of the nanotubes shows a small blue shift compared with the bulk. The photoluminescence spectrum of the nanotubes shows a band at 676 nm due to trapped states, and the band is blue-shifted with respect to that of bulk  $\text{HfS}_2$  powder (see Fig. 21a). The Raman spectrum of the  $\text{HfS}_2$  nanotubes is shown in Fig. 21b. It shows a band due to the  $A_{1g}$  mode, corresponding to the S atom vibration along the  $c$ -axis perpendicular to the basal plane, and another due to the  $E_g$  mode due to the movement of the S and Hf atoms in the basal plane.<sup>68</sup> The full-width at half maximum (FWHM) of the  $A_{1g}$  band is  $11\text{ cm}^{-1}$  in the nanotubes compared to  $8\text{ cm}^{-1}$  for the bulk sample. Such broadening of the Raman band has been noted with  $\text{MoS}_2$  and  $\text{WS}_2$  nanotubes.<sup>19</sup>

#### 4.2. $\text{ZrS}_2$ nanotubes

$\text{ZrS}_2$  nanotubes admixed with nanorods have been prepared by the thermal decomposition of  $\text{ZrS}_3$  under  $\text{H}_2 + \text{Ar}$  at 1170 K.<sup>24</sup> Many of the nanotubes exhibit rectangular tips. The inner wall of some of the  $\text{ZrS}_2$  nanotubes show non-uniformity near the tip resulting from the discontinuous growth of the  $\text{ZrS}_2$  layers.

#### 4.3. $\text{NbS}_2$ nanotubes

$\text{NbS}_3$  when heated in a stream of  $\text{H}_2$  (100 sccm) at 1000 °C for 30–60 min, produces good yield of nanostructures.<sup>23</sup> A  $c$ -axis expansion of  $\sim 3\%$  is observed in the nanotubes. The SEM image in Fig. 22a reveals a high yield of the nanostructures from the thermal decomposition of the trisulfide. These nanostructures contained a considerable amount of nanotubes as seen from the TEM images. The TEM image in Fig. 22b shows a couple of nanotubes, having closed rectangular tips. While some of the nanotubes are closed with flat non-spherical polygonal tips, most of the tubes are open at one or both ends. The image in Fig. 22c shows the high-resolution image of an open nanotube. The layer separation in the walls is  $\sim 6$  Å, corresponding to the (002) plane of bulk  $\text{NbS}_2$ . The ED pattern in the inset shows the nanotube to be single-crystalline with Bragg spots corresponding to the known  $d$  values. Some of the diffraction spots show diffuse scattering or streaking due to bent layers or disorder. The  $\text{NbS}_2$  nanostructures were not superconducting.

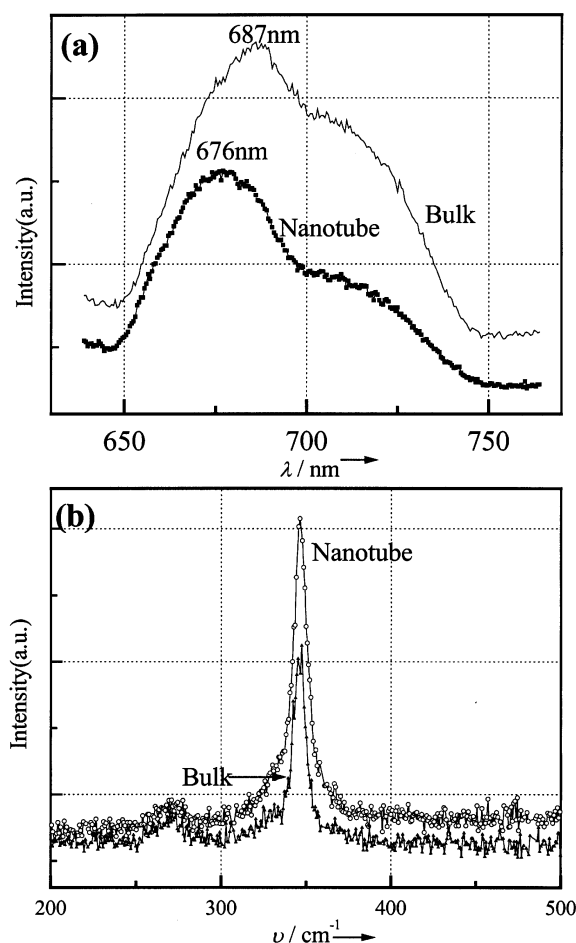


**Fig. 21** (a) Photoluminescence spectra of bulk  $\text{HfS}_2$  and  $\text{HfS}_2$  nanotubes. (b) Raman spectrum of bulk  $\text{HfS}_2$  and  $\text{HfS}_2$  nanotubes.

#### 4.4. $\text{TaS}_2$ nanotubes

$\text{TaS}_2$  nanotubes could be prepared by decomposing  $\text{TaS}_3$  at 1270 K under  $\text{H}_2$  (100 sccm). TEM observation of the product showed the presence of hollow core nanotubes in the product. The inner wall of some of the  $\text{TaS}_2$  nanotubes showed non-uniformity along the length of the tube. Some of the tubes are closed with flat rectangular tips. In both  $\text{NbS}_2$  and  $\text{TaS}_2$  nanotubes, most of the tube tips are nearly flat or rectangular.<sup>23</sup> This is in sharp contrast to the CNTs.

#### 4.5. $\text{NbSe}_2$ nanotubes

Galván *et al.*<sup>69</sup> have reported that  $\text{NbSe}_2$  nanotubes can be prepared by the use of intense electron irradiation. The nanotubes and nanorods of  $\text{NbSe}_2$  have been prepared by the decomposition of the triselenide, at  $\sim 970$  K under a gas flow of Ar.<sup>70</sup> The product contained a mixture of nanotubes and nanorods. The powder X-ray diffraction was characteristic of  $6\text{H-NbSe}_2$ , with no appreciable shift in the  $d(002)$  line position relative to the bulk sample. Most of the  $\text{NbSe}_2$  nanotubes are open-tipped. The  $\text{NbSe}_2$  nanorods generally possess smaller diameters as well as shorter lengths compared to the nanotubes. Under the most favourable conditions, the ratio of the nanotubes to nanorods was around 2 : 1. The rate of argon flow appears to have an effect on the ratio of nanotubes and nanorods in the final product. At a smaller flow rate, there was a higher percentage of nanotubes in the final product, while higher flow rates gave a greater percentage of nanorods. High argon flow also gave rise to platelets, which also occurred, on increasing the temperature.

Fig. 23a shows the HREM image of a  $\text{NbSe}_2$  nanotube in the tip region. The structure of the tip deviates from the hemi-

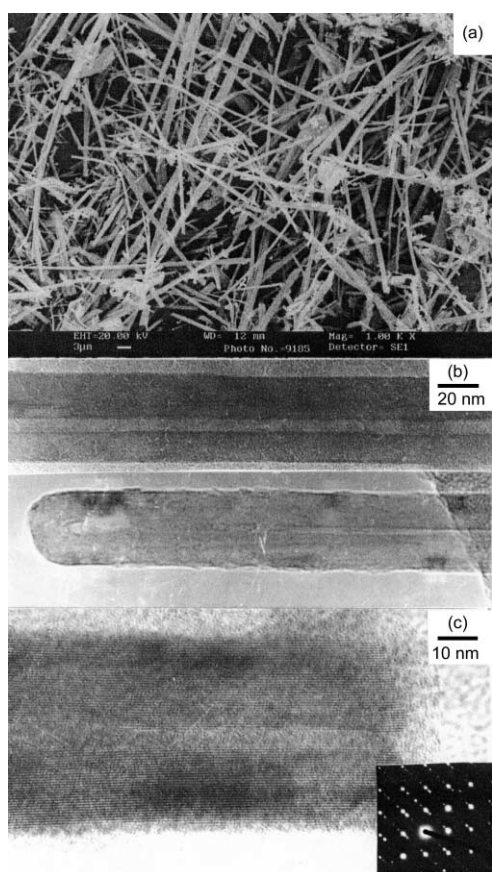


**Fig. 22** (a) SEM image of NbSe<sub>2</sub> nanotubes; (b) low-resolution TEM image and (c) HREM image of NbSe<sub>2</sub> nanotubes. Inset shows the typical ED pattern. The layer separation is 0.62 nm in the walls. (Reproduced with permission from ref. 23).

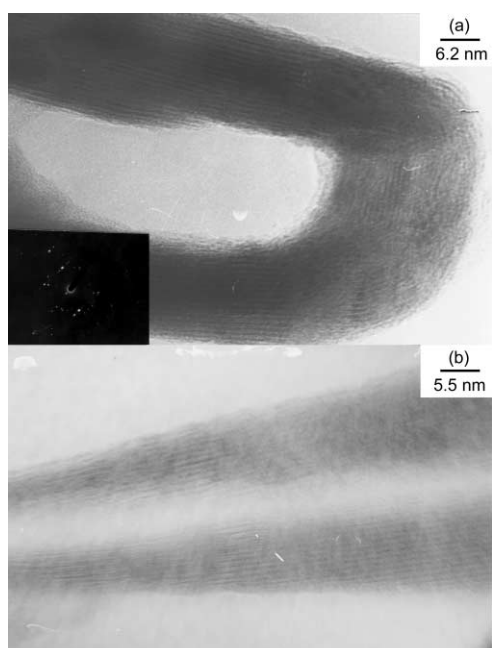


**Fig. 23** HREM images of the NbSe<sub>2</sub> nanotubes. The tube in (a) has a closed tip with a 90° bend in one corner, while the tube in (b) is near-conical in shape due to several terminated layers in the walls. The inset in (a) shows a typical ED pattern. (Reproduced with permission from ref. 70).

spherical nature, and has a 90° bend at one corner while the other corner is comparatively smooth. The outer diameter of the tube is ~57 nm and the wall contains ~16 layers. The inner wall of the tube shows evidence for terminated layer growth. Sharp facets of the type reported by Tenne *et al.*<sup>71</sup> in the fuller-

ene structures of NbS<sub>2</sub> are however not present in these nanotubes. The layers near the tip are somewhat less regularly ordered, but the number of defects, dislocations and stacking faults in the NbSe<sub>2</sub> nanotubes is generally much smaller than that in the other chalcogenide nanotubes.<sup>23,24</sup> Fig. 23b shows a HREM image of a nanotube with a near-conical closed tip showing an interlayer separation of ~6.2 Å. This tube has a tapering shape due to the disrupted growth of the layers as it proceeds towards the tip. As a result, the tube walls near the tip are thinner than that along the body of the tube. There are approximately 10 layers near the tip and ~14 layers along the body of the tube, ~77 nm away from the tip.

It is interesting that most of the NbSe<sub>2</sub> nanotubes contain more than 10 layers with one or two containing a smaller number of layers. Some of the nanotubes exhibit a different type of stacking due to the presence of different polytypes just as in BN nanotubes where the local rhombohedral stacking occurs within the hexagonal phase.<sup>44</sup>

The Raman spectrum of NbSe<sub>2</sub> single crystals exhibit three first order lines at 29.6, 230.9 and 238.3 cm<sup>-1</sup>.<sup>72</sup> The low frequency line at 29.6 cm<sup>-1</sup> is due to the rigid layer vibration mode (E<sub>g</sub><sup>2</sup>) which accounts for the weak interlayer bonding. The high-frequency lines at 230.9 and 238.3 cm<sup>-1</sup> are due to the A<sub>1g</sub> and E<sub>2g</sub><sup>1</sup> modes, respectively. The high frequency Raman modes in the NbSe<sub>2</sub> nanostructures were found to be identical to those of the bulk crystal. Bulk NbSe<sub>2</sub> shows a photoluminescence band of very weak intensity band at around 825 nm possibly due to trapped states. The band is shifted to 820 nm in the nanostructures.

NbSe<sub>2</sub> is a metallic conductor, becoming superconducting at low temperatures.<sup>3b</sup> The NbSe<sub>2</sub> nanostructures show metallic conductivity from 300 K down to lower temperatures (Fig. 24),

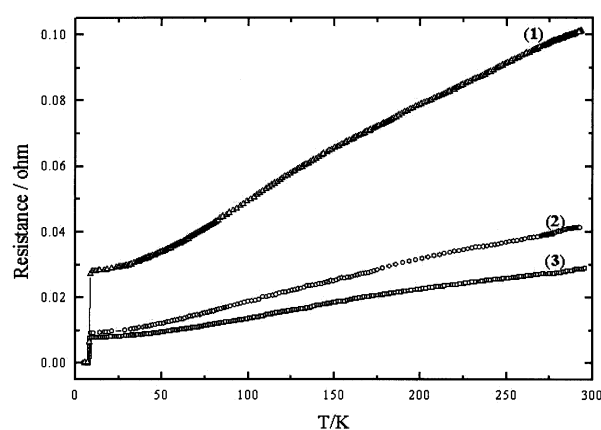


**Fig. 24** Resistance vs. temperature curves of the NbSe<sub>2</sub> nanostructures, (2) and (3), are compared with the behavior of the bulk sample in (1).

in agreement with theoretical predictions.<sup>57</sup> The resistance-temperature curve for the bulk sample has a much higher slope than for the nanostructures, possibly because of the dominance of temperature-independent scattering in the latter. The NbSe<sub>2</sub> nanostructures become superconducting at 8.3 K (Fig. 24). The superconducting transition temperature of the bulk sample was found at 8.6 K, indicating a very small decrease in *T<sub>C</sub>*, if at all, in the nanostructures. It has been suggested that the superconducting *T<sub>C</sub>* of NbSe<sub>2</sub> is dependent on factors such as stoichiometry and the number of layers of NbSe<sub>2</sub> when the number of layers goes below 6, the *T<sub>C</sub>* is expected to shift to 3 K.<sup>73</sup> The NbSe<sub>2</sub> nanostructures studied had diameters in excess of 30 nm, with the number of layers greater than 10. It would be worthwhile to prepare NbSe<sub>2</sub> nanostructures containing a smaller number of layers to study whether the *T<sub>C</sub>* is substantially affected compared to the bulk material. In this context, it must be noted that MgB<sub>2</sub> nanowires of 50–200 nm diameter



have been shown recently to have a superconducting  $T_c$  identical to that of the bulk material.<sup>74</sup>

## 5. Nanotubes of other metal chalcogenides

Nanotubes and nanowires of II–VI semiconductor compounds such as CdS and CdSe have been obtained by a soft chemical route involving surfactant-assisted synthesis.<sup>28,75</sup> For CdSe nanotubes, the metal oxide was reacted with the selenidizing reagent in the presence of a surfactant such as Triton 100X. Substantial amounts of nanotubes were obtained by this method (Fig. 25a and b). Annealing of the as-prepared nano-

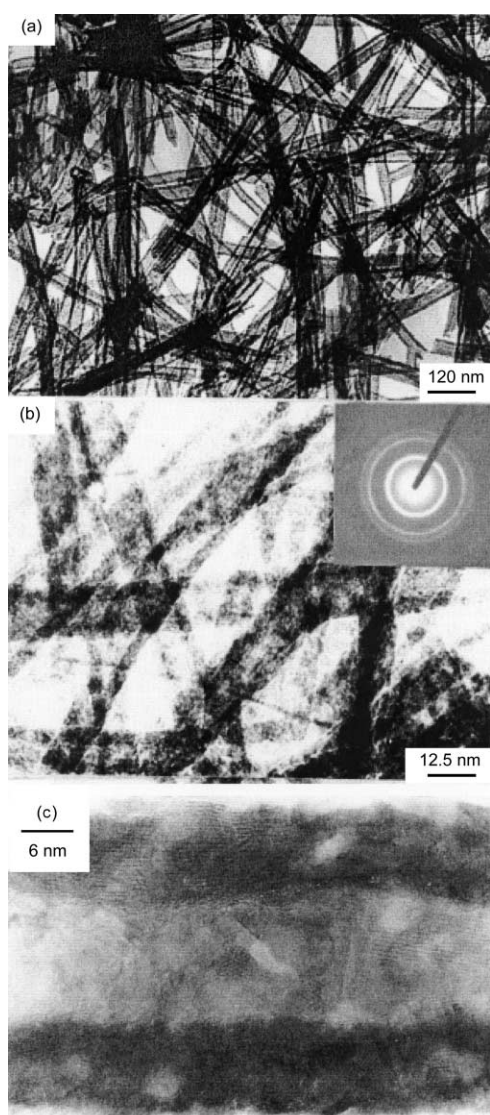


**Fig. 25** (a) and (b) low-resolution TEM images of CdSe nanotubes. Inset shows a typical ED pattern; (c) HREM image of the CdSe nanotube showing walls containing several nano-crystallites. (Reproduced with permission from ref. 28).

tubes appears to improve the crystallinity of the nanotubes (Fig. 25c). To obtain nanotubes of CdS, a similar procedure was followed, except that thioacetamide was used as the sulfidizing agent in place of NaHSe. The formation of the nanotubes and nanowires is controlled by varying the surfactant concentration which in turn changes the morphology and shape of the micellar cavity. Thus, in both CdS and CdSe, a higher concentration of the surfactants produce nanotubes, while a lower concentration of the surfactants preferentially produce nanowires. The surfactant is readily removed from the nanotubes by washing with a solvent. Both the CdSe and CdS nanotubes seem to be polycrystalline formed by aggregates of

nanoparticles.<sup>76</sup> The nanotubes of CdSe, though extended in one direction show quantum confinement and the absorption band is blue-shifted to 550 nm from 650 nm of the bulk sample. A quantum confinement effect is also observed in the PL spectrum of the nanotubes, which shows a band at 560 nm compared to 750 nm for the bulk sample (Fig. 26). The CdS nano-

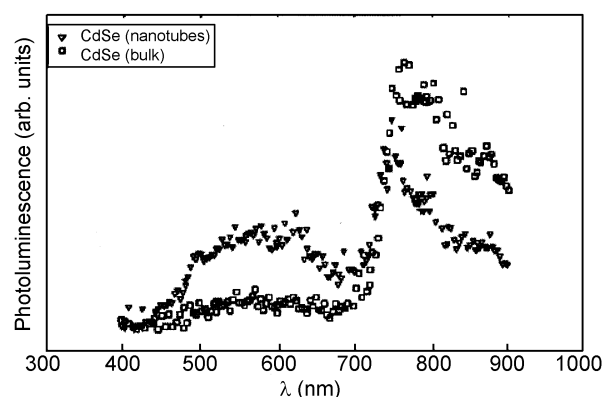


**Fig. 26** Photoluminescence spectra of nanotubes of CdSe and bulk CdSe. (Reproduced with permission from ref. 28).

tubes also show a blue-shift of the absorption maximum due to confinement effects. The Raman spectrum of CdSe nanotubes show modes at 208 and 198  $\text{cm}^{-1}$ , the former arising from the longitudinal optic phonon, red-shifted due to phonon confinement.<sup>76</sup>

ZnS nanotubes have been prepared by sulfidizing ZnO templates obtained in columnar form by electrochemical deposition.<sup>77</sup> Heating the ZnO column in  $\text{H}_2\text{S}$  above 400 °C gave the ZnS coated ZnO columns. The ZnO cores were then etched out giving hollow ZnS tubes.

Hydrothermal methods have been successfully used to synthesize a variety of nanotubes and nanorods. Layer-rolled structures of nickel sulfide have been obtained by sulfidizing the  $\text{Ni}(\text{NH}_3)_4^{2+}$  complex by  $\text{CS}_2$  in the presence of aqueous ammonia<sup>78</sup> under hydrothermal conditions. Nanotubes of  $\text{Cu}_{5.5}\text{FeS}_{6.5}$  have been prepared hydrothermally. These nanotubes are large in diameter, have thick walls and are mostly open-ended. The crystallinity of the thin-walled nanotubes is not generally satisfactory.  $\text{Cu}_{5.5}\text{FeS}_{6.5}$  has a layered structure characterized by S–S pairs and  $\text{MS}_4$  tetrahedra. The nanotubes are thought to be formed by rolling the basal planes. The ED patterns collected from the nanotubes indicates that they are of the armchair and zigzag types. In the hydrothermal synthesis of the nanotubes and related structures, organic amines seem to act as the templating agents. The amine probably intercalates into the lattice of the precursor which is subsequently decomposes to yield the chalcogenide nanotubes around the templating amine.

## 6. Metal oxide nanotubes

Metal oxide nanotubes have been prepared by using a variety of techniques including templating reactions, sol–gel chemistry and hydrothermal methods.<sup>7</sup> Besides CNTs, organic surfactants have been employed to grow oxidic nanotubes. Pores of anodic alumina have been used as confining templates for the growth of  $\text{TiO}_2$  and  $\text{Al}_2\text{O}_3$  nanotubes, as well as coaxial nanotubes of  $\text{TiO}_2$  sheathed  $\text{SiO}_2$ .<sup>80,92</sup>

### 6.1. $\text{VO}_x$ nanotubes

Vanadium oxides deserve special attention owing to their structural flexibility and interesting catalytic, electrochemical and other properties.  $\text{V}_2\text{O}_5$  can be regarded as a layer structure in which the  $\text{VO}_5$  square pyramids are connected by sharing

corners and edges and thereby forms the layer.<sup>81</sup> The interlayer interaction is weak as shown by the long V–O distances.<sup>82</sup> This structural characteristic permits the intercalation of various cationic species in the interlamellar space.<sup>83</sup> The cations include alkylammonium ions which are readily intercalated in between the layers under hydrothermal conditions.<sup>84</sup> Thus, this system is analogous to graphite and the layered dichalcogenides. In 1998 Nesper and co-workers<sup>11,85</sup> synthesized nanotubules of alkylammonium intercalated  $\text{VO}_x$  by hydrothermal means. The vanadium alkoxide precursor was hydrolyzed in the presence of hexadecylamine and the hydrolysis product (lamellar structured composite of the surfactant and the vanadium oxide) yielded  $\text{VO}_x$  nanotubes along with the intercalated amine under hydrothermal conditions (Fig. 27). The interesting feature of this

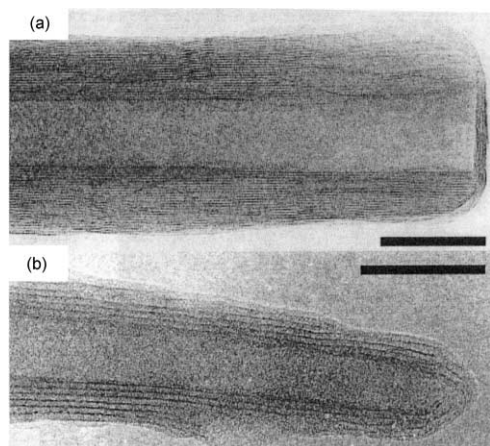


**Fig. 27** TEM images of  $\text{VO}_x$  nanotubes with intercalated amine having varying chain lengths; (a)  $\text{C}_4\text{VO}_x\text{-NT}$ ; (b)  $\text{C}_{16}\text{-VO}_x\text{-NT}$ . The length of the bar is 50 nm. (Reproduced with permission from ref. 85).

vanadium oxide nanotube is the presence of vanadium in the mixed valent state, thereby rendering it redox-active. The template could not be removed by calcination as the structural stability was lost above 523 K. Nevertheless, it was possible to partially extract the surfactant under mildly acidic conditions. These workers have later shown that the alkylamine intercalated in the intertubular space could be exchanged with other alkylamines of varying chain lengths as well as  $\alpha,\omega$ -diamines.<sup>85</sup> The distance between the layers in the  $\text{VO}_x$  nanotubes can be controlled by the length of the  $-\text{CH}_2-$  chain in the amine template. The tubes obtained with the diamine had thicker walls compared to those obtained with the monoamines. A change in the interlayer distance observed in the XRD pattern as a function of the alkyl chain length is rendered to be due to the monolayer arrangement of the amine molecules in between the layers. In the  $\text{VO}_x$  nanotubes, the amine may be acting as a structure-directing agent and is incorporated in the tube walls.

Most of the  $\text{VO}_x$  nanotubes obtained by the hydrothermal method are open-ended. Very few closed tubes had flat or pointed conical tips. Cross-sectional TEM images of the nanotubular phases show that instead of concentric cylinders, (*i.e.* layers that fold and close within themselves), the tubes are made up of single or double layer scrolls providing a serpentine-like morphology.<sup>85,86</sup> The scrolls are seen as circles that do not close in the images (Fig. 28). Non-symmetric fringe patterns in the tube walls exemplify that most of the nanotubes are not rotationally symmetric and carry depressions and holes in the walls. Diamine-intercalated  $\text{VO}_x$  nanotubes are multilayer scrolls with narrow cores and thick walls, composed of packs of several vanadium oxide layers (Fig. 29). The diamine-containing  $\text{VO}_x$  nanotubes also show a smaller number of holes in the wall structure and the tubes are well ordered with uniform distances throughout the tube length.<sup>85</sup> The scroll-like structure of the nanotubes may be the most obvious cause for their high structural flexibility. This is also why facile exchange reactions occur.

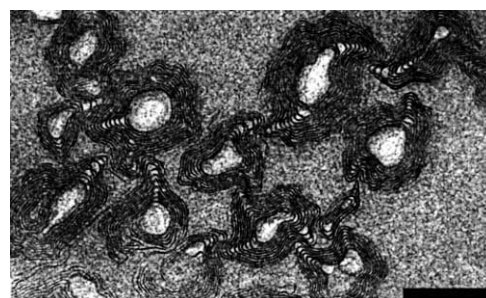


**Fig. 28** Cross-sectional TEM images of monoamine-intercalated  $\text{VO}_x$  nanotubes showing serpentine-like scrolls.

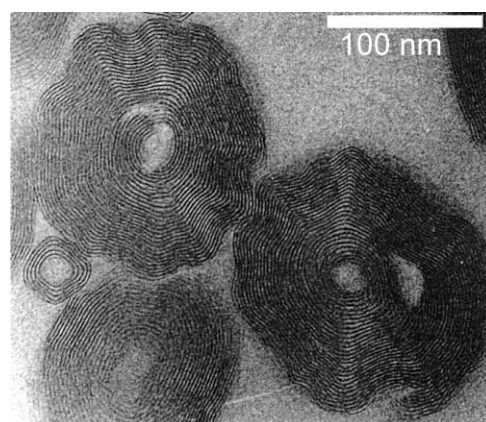


**Fig. 29** Cross-sectional TEM images of diamine-intercalated  $\text{VO}_x$  nanotubes showing a larger thickness of the tube walls and a smaller inner core. (Reproduced with permission from ref. 85).

It must be pointed out that the  $\text{VO}_x$  scroll-like structures are not genuine nanotubes of the type formed by carbon or metal dichalcogenides.

The alkylammonium intercalated  $\text{VO}_x$  nanotubes are paramagnetic and show semimetallic conductivity probably due to the mixed valent V centers. The percentage content of V(IV) calculated on the basis of the effective magnetic moment is ~45–50%.<sup>85</sup> The structure contains  $\text{VO}_4$  tetrahedra and  $\text{VO}_5$  square-pyramids simultaneously.

The as-synthesized amine intercalated  $\text{VO}_x$  nanotubes could be aligned on glass substrates by using micromolding in capillaries (MIMIC).<sup>86</sup> An elastomeric polydimethylsiloxane (PDMS) stamp where parallel capillaries of 5  $\mu\text{m}$  were patterned was used as the mould.<sup>86</sup> The capillaries were filled with a  $\text{VO}_x$  nanotube suspension in octanol. After evaporation of the solvent and removal of the mould, long lines of assemblies of well aligned nanotubes were obtained.

Vanadium oxide nanotubes containing primary monoamines with long alkyl chains have been prepared by employing non-alkoxide vanadium precursors such as  $\text{VOCl}_3$  and  $\text{V}_2\text{O}_5$ . The amine complexes of the vanadium precursors are then hydrolyzed. Hydrothermal treatment of the precursors gives good yields of  $\text{VO}_x$  nanotubes incorporating the amines.<sup>27</sup> The distance between the layers is proportional to the length of the alkyl amine chain which acts as the structure-directing template. Cross-sectional TEM images demonstrate the predominance of serpentine-like scrolls rather than of concentric tubes.

Mn–V-oxides have been prepared starting from vanadium oxide–dodecylamine composite nanotubes.<sup>87</sup> The composite nanotubes were prepared by mixing  $\text{V}_2\text{O}_5$  with dodecylamine in the presence of ethanol and water. The amine templates can be easily substituted or even ion-exchanged with ions like  $\text{Mn}^{2+}$  in an aqueous alcohol solution to obtain the Mn–V–O nanotubes. Most of the nanotubes had open ends, while some of them had closed ends, with the side of the tubes wrapped around the end to close it. The  $\text{Mn}^{2+}$  ions replace the organic cations in the structures and hence are intercalated in between the layers.



## 6.2. Use of carbon nanotubes as templates for the growth of oxide nanotubes

Carbon nanotubes have been successfully used as removable templates for the synthesis of a variety of oxide nanotubes. Ajayan *et al.*<sup>9</sup> reported the preparation of  $V_2O_5$  nanotubes by using partially oxidized carbon nanotubes as templates. Apart from coating of CNTs by the oxide phase, metal oxide fillings in the internal cavities and thin oxide layers between the concentric shells of the tubes were also obtained (Fig. 30). A mix-

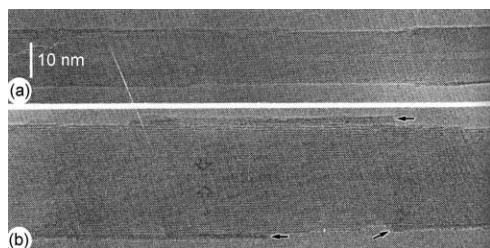


**Fig. 30** TEM images of the  $VO_x$  coated carbon nanotubes. (a) Low-magnification image showing partial coating; (b) image at higher magnification showing the 0.34 nm fringes of the CNT and oxide coatings of uniform thickness on the upper and lower parts of the tubes. (Reproduced with permission from ref. 9).

ture of partially oxidized CNTs and  $V_2O_5$  powder was annealed in air to produce a nanotube–oxide composite. The external coating of the tubes consists of crystalline  $V_2O_5$  layers, which grow with the *c*-axis parallel to that of the nanotube layers. Intercalation of the oxide occurs where there are missing shells of the nanotubes. The coating on the isolated nanotubes is of uniform thickness, but does not always cover the entire length of the nanotube surface. Continuous cylindrical oxidic films on the nanotube surface are generally formed over a length of a few hundred nanometers. Attempts have been made to remove the carbon nanotube templates by oxidation at 650 °C. These samples show a dramatic increase in the ratio of the coated to the uncoated tubes. On observing the tips of the remaining coated tubes, oxidation was found to have occurred from the inner wall of the tube and progressed outwards leaving few outer layers and the outer coating of the oxide. This is in contrast to the oxidation of pure nanotubes where the etching of the layers starts from outside and proceeds inwards leaving chisel-shaped tips. The complete removal of the nanotube template resulted in larger hollow oxidic structures with thin skins.

Rao *et al.*<sup>10</sup> have prepared a variety of oxide nanotubes including  $SiO_2$ ,  $Al_2O_3$ ,  $V_2O_5$ ,  $MoO_3$  and  $RuO_2$  employing carbon nanotube templates. By using multi-walled carbon nanotubes as the template they also made nanotubes of zirconia and yttrium-stabilized zirconia.<sup>30</sup> In these preparations, acid-treated MWNT bundles were coated with a suitable precursor of the metal oxide, and the coated composites heated to high temperatures to remove the carbon template (Fig. 31). TEM images show that the carbon nanotubes get fully coated with the oxidic material on reaction with the organometallic compound followed by calcination at 500 °C. The nanotube features are essentially retained in the oxide–nanotube composites even after calcination at 500 °C (Fig. 31). Acid-treated tubes give a better coating than the pristine ones. The nanotube templates could be removed successfully by heating at 750 °C for several hours. The oxidation proceeded from the hollow regions inside the tubes. Silica nanotubes prepared by this method could be modified by doping with transition metal ions for possible use in catalysis. Thus Cu, Cr or Ni containing  $SiO_2$  tubes have been prepared by this method by taking the relevant transition metal ions in the starting reaction mixture.<sup>10</sup> The transition metals are present as oxides in the final structure, and the oxide appeared as islands on the surface of the hollow silica tubes in the case of Cu.

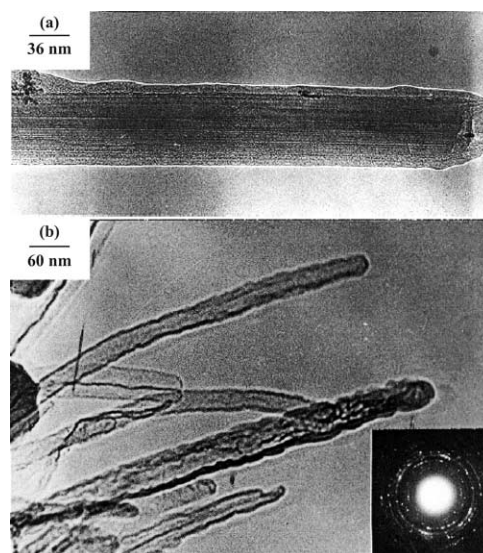


**Fig. 31** (a) TEM image of a  $ZrO_2$  coated CNT. (b) Hollow  $ZrO_2$  nanotubes after removal of the CNT template. (Reproduced with permission from ref. 30).

## 6.3. $TiO_2$

Nanotubes of transition metal oxides that do not possess layered structures, (*e.g.*,  $TiO_2$ ,  $ZrO_2$ ) have been prepared by employing the sol–gel technique, membrane-confined growth and templated growth. Titania tubes were first prepared electrochemically by Hoyer.<sup>88</sup> A polymer mould with a negative (replicated) structure of an anodic alumina porous membrane was used for electrodeposition of the titania nanotubes. The titania phase obtained was amorphous and calcination to induce crystallization led to the deformation of the tube structure. The diameters of the tubes were in the ~70–100 nm range, being controlled by the pore size of the membrane. Needle-shaped anatase nanotubes could be precipitated from a gel containing a mixture of  $SiO_2$  and  $TiO_2$ .<sup>29</sup> A mixture of titanium isopropoxide and tetraethylorthosilicate (TEOS) was hydrolyzed and gelled in an incubator, and the gel further heated to 870 K resulting in the precipitation of fine  $TiO_2$  (anatase) crystals. This was further treated with NaOH at 380 K for 20 h to yield the  $TiO_2$  nanotubular phase. An amorphous  $SiO_2$ -related phase present in the product could be removed by chemical treatment. The nanotubes formed by this method had a diameter of ~8 nm and lengths upto 100 nm (Fig. 32a).

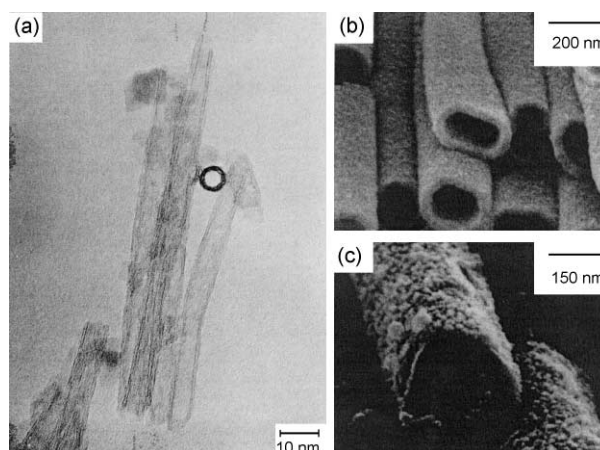


**Fig. 32** (a) TEM image of  $TiO_2$  nanotubes (Reproduced with permission from ref. 29); (b) and (c) FE-SEM images of  $TiO_2$  nanotubes deposited from a  $TiF_4$  solution. (Reproduced with permission from ref. 80).

Titania nanotubes are obtained by the direct deposition of titanium tetrafluoride ( $\text{TiF}_4$ ) in the pores of an alumina membrane.<sup>80</sup> The porous alumina membrane prepared electrochemically was immersed in an aqueous solution of  $\text{TiF}_4$  and ammonia, and maintained at 60 °C. The walls of the nanotubes contained small nanoparticles of anatase (Fig. 32b). Titania rods were obtained at longer deposition times. The initial solution supersaturated with titania produces nuclei of anatase which deposit on the inner walls of the porous membranes, and give rise to the nanotubes. Photocatalytic activity of the as-deposited anatase nanotubes shows a performance similar to that of the conventionally prepared anatase powder.<sup>80</sup> Titania nanotubes are also prepared by using electrospun polymer fibers as templates.<sup>89</sup> The polymer fibers are coated with titanium oxide, by dipping in a titanium isopropoxide solution followed by dipping in ethanol–water for hydrolysis and condensation. Thermal treatment of the metal oxide coated polymer fibers results in the loss of the polymeric core, producing hollow nanotubes of titania. HREM images show that the individual particles that make the nanotube walls are crystalline (anatase phase). The sol–gel coating was able to mimic the finer details of the polymeric fiber, thereby forming nodules in the inner walls of the tubes. Well aligned, uniform arrays of titania nanotubes could be fabricated by the anodic oxidation of a pure Ti sheet in an aqueous solution containing 0.5 to 3.5 wt% of  $\text{HF}$ .<sup>90</sup> The upper ends of these tubes were mostly open. Recently, single crystalline nanotubes of  $\text{TiO}_2$  (anatase) have been prepared by an unconstrained solution growth, by hydrolyzing  $\text{TiF}_4$  under acidic conditions at 60 °C (Fig. 33).<sup>91</sup> A majority of these  $\text{TiO}_2$  nanotubes were closed, with spherical or polyhedral caps.

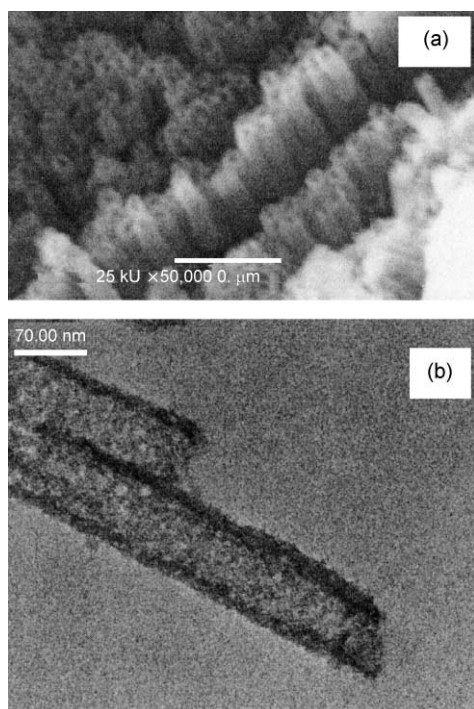


**Fig. 33** (a) SEM image of unidirectionally aligned  $\text{TiO}_2$  nanotubes; (b) TEM image of a  $\text{TiO}_2$  nanotube formed with nanocrystalline  $\text{TiO}_2$  particles. (Reproduced with permission from ref. 91).

Pores of anodic alumina have been used for the growth of coaxial nanotubes of  $\text{TiO}_2$  sheathed  $\text{SiO}_2$ .<sup>92</sup> Electrochemical deposition in the pores of a polymeric alumina membrane generates arrays of  $\text{TiO}_2$  nanotubes. For the coaxial nanotubes, the  $\text{SiO}_2$  nanotubes are first grown inside the pores of the anodic alumina membrane. The  $\text{TiO}_2$  nanotubes are then grown inside the  $\text{SiO}_2$  nanotubes. The existence of  $\text{Ti-O-Si}$  bonds in the amorphous sheaths is believed to play a role in the formation of these composite nanotubes.

## 6.4. $\text{SiO}_2$ and $\text{Al}_2\text{O}_3$ nanotubes

**6.4.1.  $\text{SiO}_2$ .** Sol–gel techniques have been extensively used to form silica gel nanotubes<sup>93</sup> as well as mesoporous silica nanotubes.<sup>25</sup> Nakamura and Matsui<sup>93</sup> prepared silica nanotubes as a spin-off product of sol–gel synthesis wherein, tetraethylorthosilicate (TEOS) was hydrolyzed in the presence of ammonia and D,L-tartaric acid. Mesoporous silica nanotubes were also prepared by a special post-synthesis-ammonia-hydrothermal treatment of the mesoporous silica material.<sup>25</sup> It was possible to simultaneously restructure the pore size, nanochannel regularity and morphology of the mesoporous material by this method. The restructured products were highly ordered and exhibited nanotubular forms of silica. This methodology gained momentum with the successful synthesis of individual nanotubes or small bundles containing a few nanotubes. Adachi *et al.*<sup>94</sup> were the first to report the synthesis of very long silica nanotubes by employing surfactant-assisted growth. Laurylamine hydrochloride was used as the surfactant template around which TEOS was hydrolyzed. Tube formation was followed by trisilylation treatment. Trimethylsilylation inactivated the silanol groups on the surface of the tube, thus inhibiting the condensation of silanol groups between the different bundles, and yielding long individual silica tubes. Another advantage of the trisilylation treatment was that the surfactant was removed without calcination. Individual silica nanotubes have also been prepared by the sol–gel method in the presence of citric acid as the structure modifier.<sup>95</sup> The silica nanotubes obtained were, however, mostly amorphous as determined by XRD. Electron microscopy revealed that the individual silica nanotubes were long (~0.5–20  $\mu\text{m}$ ), with wide diameters.

The sol–gel technique has been used to dope silica in  $\text{TiO}_2$  nanotubes.<sup>96</sup> Different loadings of Si in the  $\text{TiO}_2$  nanotubes was achieved by varying the amount of TEOS in the starting solution containing tetrapropylorthotitanate in butanediol. After several days of aging the dry gel was calcined to induce the crystallization and formation of the nanotubes. The pore size of the nanotubes decreased with increasing Si content. EDAX mapping images revealed that the Ti and Si were homogeneously distributed in the nanotubes. It is believed that Si doping influences the sintering process and suppresses the grain growth of titania nanoparticles, thus increasing the surface area of the doped tube.<sup>96</sup>

Mesoporous silica materials with hierarchical tubule-within-tubule structures have been prepared and characterized by spectroscopic methods.<sup>97</sup> Strong photoluminescence of these materials is explained as due to the presence of  $\text{Si-OH}$  complexes located on the nanotube surface, which also explains the persistence of the signal for some time after the pumping laser is turned off.

**6.4.2.  $\text{Al}_2\text{O}_3$ .** Alumina nanotubes have been prepared by electrochemical means.<sup>12</sup> Two different preparation methods designated as normal stepwise anodization (NSA) and lateral stepwise anodization (LSA) have been employed for the purpose. The major difference between the two methods is the way the potential was applied. An aluminium film deposited on a p-type Si substrate was anodized in dilute  $\text{H}_2\text{SO}_4$ . In NSA, the potential was applied to the bottom surface of the Si substrate, while in LSA, it was applied to the top surface of the alumina film. The nanotubes formed were attached to the anodic porous alumina film (Fig. 34a). The NSA tubes were smaller than the LSA tubes. In addition to straight alumina nanotubes, branched alumina nanotubes were also obtained in the same synthesis (Fig. 34b).<sup>12,98</sup>

## 6.5. Other oxide nanotubes

Recently, ZnO nanotubes have been prepared hydrothermally.<sup>99</sup> In this procedure, ethanol was added to an aqueous solution containing the  $\text{Zn}(\text{NH}_3)_4^{2+}$  complex, and the mixture heated to



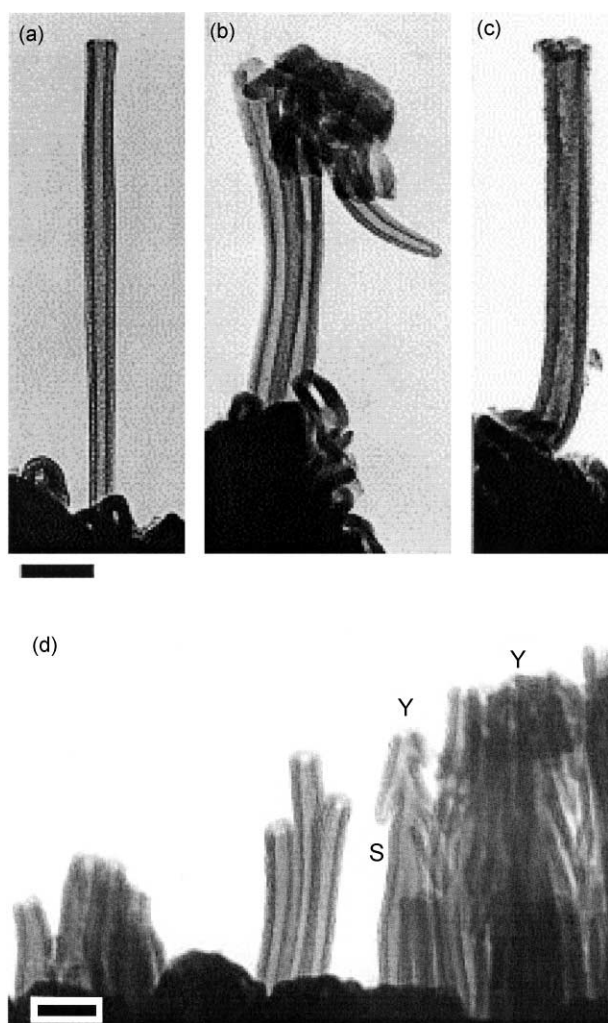


**Fig. 34** TEM images of alumina nanotubes: (a and b) NSA tubes; (c) LSA tubes; (d) side-view of the branched alumina tubes attached to the APA film, (Y indicates Y-shaped branched cells, S indicates the stem of such branched cells). (Reproduced with permission from refs. 12 and 98).

450 K for 13 h in a Teflon-lined autoclave. There was, however, deviation in the peak intensities compared to the standard diffraction pattern, indicating the preferred orientation of the tubular ZnO (wurtzite). TEM images showed that the walls of the ZnO tubes were not very smooth due to the build-up by polycrystalline nanoparticles. The  $\text{Zn}(\text{NH}_3)_4^{2+}$  complex is hydrolyzed in the presence of ammonia and nanoparticles of ZnO are produced along with the nanotubes as seen in the TEM images. As the temperature and duration of the reaction are increased, there is increased evolution of ammonia and the ZnO nanoparticles assemble along certain orientations and aggregate to the hollow tubular structures.

Oxides of Er, Tm, Yb and Lu have been prepared in the nanotubular form employing template-mediated reactions using dodecylsulfate assemblies.<sup>100</sup> These oxodic nanotubes were synthesized by the homogeneous precipitation method using urea. The oxodic phase was precipitated from the reaction mixture containing the salt of the rare earth element, sodium dodecylsulfate and water, the pH of the medium being varied by the progressive addition of urea. Hydrolysis of the rare earth salt occurs on heating to 60 °C and the oxodic phase forms a precipitate. The rare earth oxide nanotubes so obtained have small inner diameters and thin walls. Only Yb- and Lu-oxide nanotubes have been obtained reproducibly by this method.

Nanotubes of  $\text{In}_2\text{O}_3$  and  $\text{Ga}_2\text{O}_3$  have been synthesized by employing sol-gel chemistry and porous alumina templates.<sup>101</sup> Aqueous ammonia is added to In (or Ga) containing sols to

obtain precipitates which are then peptized with nitric acid to produce stable sols. The alumina membrane is immersed in the sol and then air-dried followed by annealing in air at elevated temperatures for 12 h to obtain the oxides. The alumina template is dissolved in alkali solution to give the free tubes. The hollow nanotubes so obtained have lengths of upto 10  $\mu\text{m}$ . The inner diameters could be varied by selecting the template dimensions and the immersion time. The positively charged sol particles adhere to the negatively charged pore walls of the templating membrane leading to the formation of alumina-semiconductor composite nanotubes after annealing.

Nanotubes of perovskite oxides have been prepared by employing a template-mediated growth mechanism.<sup>102</sup> Nanotubes of the ceramic materials such as  $\text{BaTiO}_3$  and  $\text{PbTiO}_3$  are obtained by heating the metal acetate sol with Ti-isopropoxide in ethanol. Masked Whatman anodic membranes (200 nm pores) were used as the templates and were immersed in the mixed sol, and then air-dried. The templates could be removed after calcination followed by treatment with 6 M NaOH. TEM images revealed 50  $\mu\text{m}$  long  $\text{BaTiO}_3$  tubes bundled together after removal of the template. Most of the tubes obtained were open-ended (Fig. 35). Nanotubes of both  $\text{PbTiO}_3$  and  $\text{BaTiO}_3$

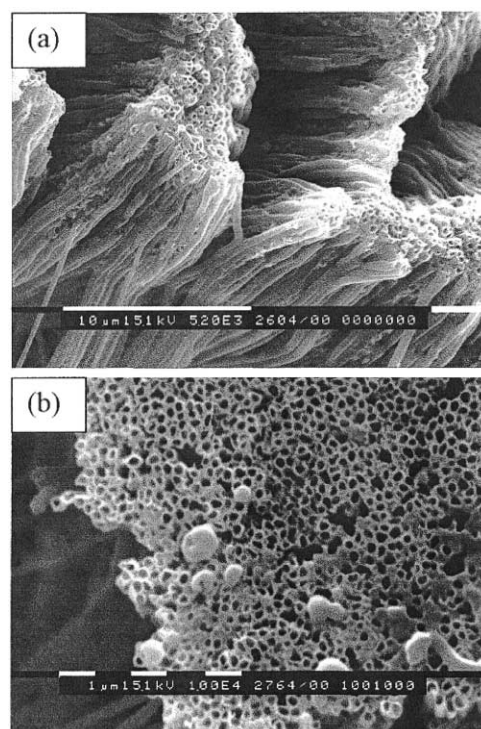


**Fig. 35** SEM images of the perovskite nanotubes: (a) side-view showing the bundle formation after removal of the template; (b) top-view of  $\text{PbTiO}_3$  bundles showing the open ends. (Reproduced with permission from ref. 102).

were found to be hollow throughout their length. XRD, Raman and electron diffraction measurements indicated that  $\text{BaTiO}_3$  was in the cubic (paraelectric) phase, while  $\text{PbTiO}_3$  was in a tetragonal ferroelectric phase after calcination. TEM images also showed that the tubes comprise small polycrystalline grains.

## 7. Nanotubes of BN and other nitrides

Based on theoretical calculations, the existence of nanotube structures of BN was predicted in 1994<sup>13,103</sup> which was soon verified by the first synthesis of BN nanotubes in 1995.<sup>104</sup> Based on theoretical calculations, it was predicted that unlike the carbon nanotubes whose electronic properties (metallic or semi-

conducting nature) are controlled by the tube diameter, wrapping, twisting and topological defects, the electronic properties of the BN nanotubes were independent of the tube diameter and chirality. In contrast to the CNTs, the BN nanotubes were predicted to be constant band-gap materials, with a large band gap of  $\sim 5.5$  eV.<sup>13</sup>

Thin BN tubes of less than 200 nm diameter were obtained by arc discharge with hollow tungsten electrodes filled with h-BN powder. Following this initial report, a variety of methods have been employed to prepare BN nanotubes. In some cases, BN nanocages and fullerenes were also obtained.<sup>105</sup> The methods of synthesis of BN nanotubes include those which are far from the equilibrium, such as the electrical arc method,<sup>32,104</sup> arcing between h-BN and Ta rods in a N<sub>2</sub> atmosphere,<sup>106</sup> laser ablation of h-BN,<sup>107</sup> and continuous laser heating of h-BN surfaces.<sup>108</sup> The last method is particularly useful in providing long ropes of BN nanotubes with thin walls. Faceted BN polyhedra filled with metallic boron are found in a few cases. Single-walled BN nanotubes are also observed in some cases.<sup>32,109</sup> Recently, single-walled nanotubes of BN deposited on polycrystalline W substrates were obtained by using electron-cyclotron resonance nitrogen and electron beam boron sources.<sup>110</sup> Fig. 36 shows a

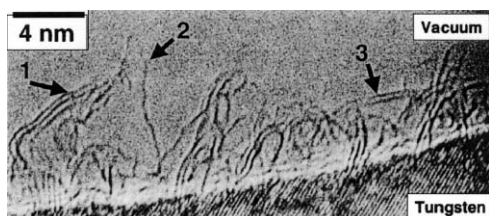


**Fig. 36** HREM image of single-walled BN nanotubes adhering on a W substrate. (Reproduced with permission from ref. 110).

HREM image of the single-walled BN nanostructures adhering to the W substrate. *In-situ* HREM images show that the single-walled BN nanotubes contain both four- and eight-fold rings and the tubes are closed with fullerene-like structures. This is in contrast to the rectangular terminations observed earlier<sup>109</sup> which were interpreted in terms of the closure *via* four-fold rings and by nitrogen-rich pentagons.

Boron nitride nanotubes co-existing with a web and an amorphous phase were obtained by a plasma jet method wherein a sintered BN disk was subjected to a direct current arc plasma jet with Ar-H<sub>2</sub> as the plasma gas.<sup>111</sup> As revealed by the HREM image (Fig. 37), the tubes grow from the amorphous phase present at the root of the tubes. The tubes were closed by parallel bases of co-axial cylindrical shape. Solid state processes have also been employed to obtain BN nanotubes. Hexagonal BN powder was first ball-milled to generate highly disordered and amorphous nanostructures which were then annealed under N<sub>2</sub> to 1570 K for about 10 h.<sup>112</sup> Several tubes with bamboo-like morphology were observed some of which contained metal particles at the tip as a contaminant from the stainless steel reaction chamber. The nanostructure of the ball-milled powder which acts as the catalyst was crucial for the tube growth.

Apart from the above methods, some of which employ drastic conditions, processes close to equilibrium conditions such as pyrolysis and chemical vapor deposition (CVD) have also been employed to prepare BN nanotubes. The CVD growth of hollow, crystalline BN nanotubes by the pyrolysis of borazine on nickel boride catalyst particles maintained at 1270–1370 K, produced nanotubes with bulbous or flag-like encaps (Fig. 38).<sup>16b</sup> The reaction is given by,



A root-growth mechanism has been proposed for the growth of BN nanotubes, wherein the nanotubes nucleate on the nickel boride catalyst particle often with irregular initiation caps and

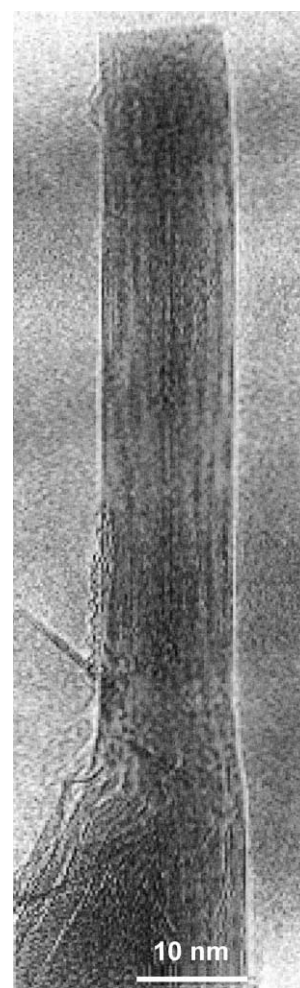


**Fig. 37** TEM image of a BN nanotube having a phase boundary between the amorphous phase and the nanotube structure at the roots. (Reproduced with permission from ref. 111).

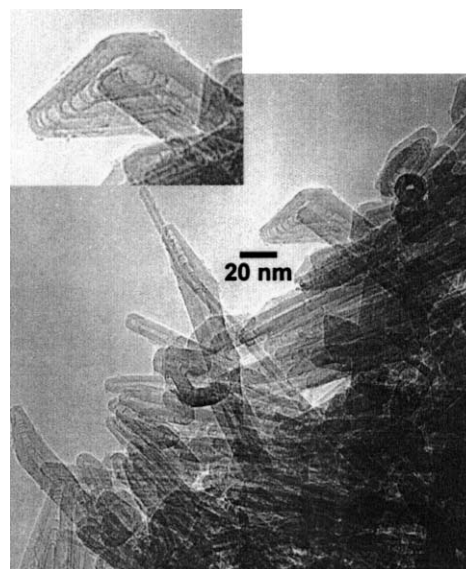


**Fig. 38** TEM image showing different BN nanotube tip closures. The club-shaped tip is magnified in the inset. (Reproduced with permission from ref. 16b).

grow out by the incorporation of additional BN at the catalyst–nanotube junction. An efficient CVD method involving the thermal decomposition of the 1 : 2 adduct of melamine and boric acid in a N<sub>2</sub> atmosphere at 1970 K was developed for the synthesis of BN nanotubes. This method does not use any metal catalyst.<sup>16c</sup> The nanotubes have the stoichiometric composition and the HREM images (Fig. 39a) reveal the regular



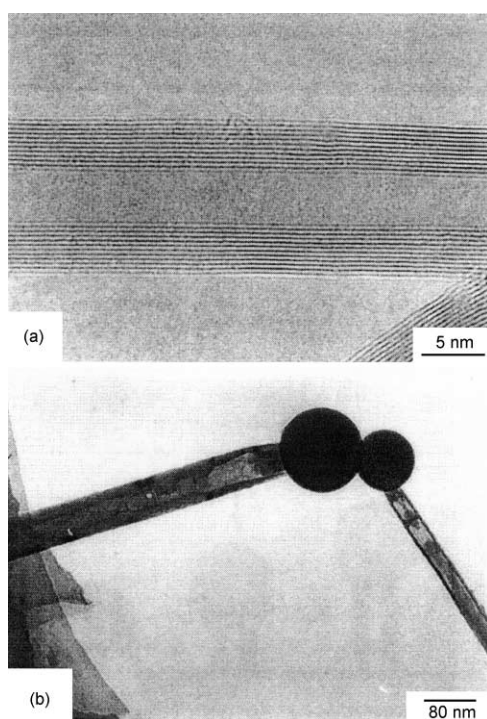


**Fig. 39** (a) HREM image of a multi-walled BN tube (layer separation = 5.2 nm); (b) low-magnification image of the tubes showing that they may grow out from the bulbous tips. (Reproduced with permission from ref. 113).

spacing of the BN layers ( $d = 5.2$  nm). The nanotubes had bulbous tips filled with amorphous material (Fig. 39b) and the tip-growth mechanism seems to be valid. The amorphous material contains mainly  $B_4N_3O_2H$ .<sup>113</sup> It is believed that at the reaction temperature (1700 °C), some species such as  $B_2O_3$  form along with the amorphous B–N–O cluster originating from decomposition of the precursor. The BN nanotube growth from the oxide phase follows the reaction



Boron powder has also been used in the CVD method for growing BN nanotubes. By heating a mixture of B and iron oxide in flowing ammonia gas, nanotubes and nano-bamboo structures of BN were obtained.<sup>114</sup> The *in-situ* generated Fe particles act as a catalyst and the growth of the BN nanotubes and nano-bamboo structures is ascribed to the vapor–liquid–solid (VLS) catalytic growth mechanism. Recently,  $B_2O_2$  (obtained by heating B and MgO at 1300 °C) was heated in the presence of  $NH_3$  in a BN-made reaction tube, to obtain BN nanotubes as the product with ~40% yield.<sup>115</sup> Most of the nanotubes obtained were open-tipped showing irregular fracture surfaces.

An exhaustive study has been carried out recently on the synthesis of BN nanotubes and nanowires by various CVD techniques.<sup>17</sup> The methods examined include heating boric acid with activated carbon, multi-walled carbon nanotubes, catalytic iron particles or a mixture of activated carbon and iron particles, in the presence of ammonia. With activated carbon, BN nanowires are obtained as the primary product. However, with multi-walled carbon tubes, high yields of pure BN nanotubes are obtained as the major product. BN nanotubes with different structures were obtained on heating boric acid and iron particles in the presence of  $NH_3$ . Aligned BN nanotubes are obtained when aligned multi-walled nanotubes are used as the templates (Fig. 40). Prior to this report, alignment of BN nanotubes was achieved by the synthesis of the BN nanotubule composites in the pores of the anodic alumina oxide, by the decomposition of 2,4,6-trichloroborazine at 750 °C.<sup>116</sup> Attempts had been made earlier to align BN nanotubes by

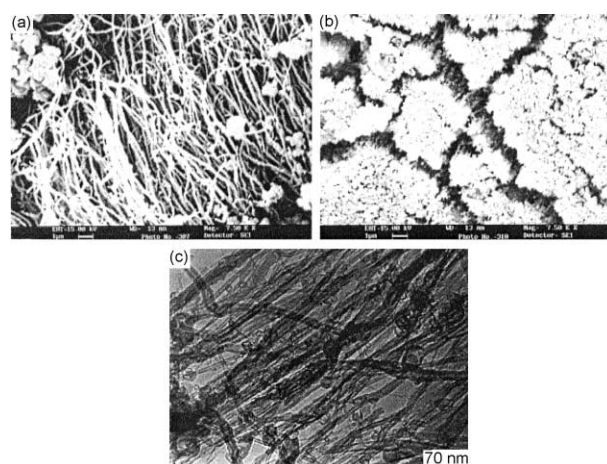


**Fig. 40** SEM and TEM images of aligned BN nanotubes: (a) and (b) give side and top view SEM images, respectively; (c) TEM image of pure BN nanotube. (Reproduced with permission from ref. 17).

depositing them on the surfaces of carbon fibers.<sup>113</sup> The tubes grow almost vertically from the surface and are nearly aligned.

Carbon nanotubes have been used successfully as templates for the growth of BN nanotubular structures.<sup>15,17,117</sup> MWNTs were heated to 1773 K with  $B_2O_3$  in a  $N_2$  atmosphere. Several metal oxides like  $MoO_3$ ,  $V_2O_5$ ,  $Ag_2O$  or  $PbO$ <sup>118</sup> were used as growth promoters, and added separately into the starting powder mixtures. Pyrolysis of borazine in the presence of acetylene over metal catalyst particles yielded B–C–N nanotubes.<sup>15a</sup> Previously  $B_xC_yN_z$  nanotubules were prepared by the arc-discharge method.<sup>14a</sup> B–C–N composite rods were used as the anode and arced against pure graphite cathodes in a He gas environment to yield the nanotubules.

Boron nitride nanotubes have been used in a wide variety of ways to generate nanocables where the BN nanotubes play host to 1D nanowires or nanoclusters occupying the hollow cavity. Zhang and co-workers<sup>119</sup> have reported the synthesis of  $(BN)_x C_y$  nanotubes filled with a SiC and  $SiO_2$  core by laser ablation. Carbon nanotube-confined reactions involving substitution reactions are employed to synthesize SiC nanowires encapsulated in BN nanotubes.<sup>120</sup> The CNTs react with boron oxide vapor in the presence of  $N_2$  to yield BN nanotubes. The SiO vapor then penetrates into the cavity of the nanotubes and reacts with the internal wall of the CNTs to give SiC nanowires. In some cases, the filling occurs through the entire length of the nanotube. In a slightly modified method, BN and  $(BN)_x C_y$  nanotubes filled with boron carbide nanowires were prepared using CNTs as templates.<sup>121</sup> The  $(BN)_x C_y$  nanotubes are formed by capillary filling of boron oxide vapor in the inner cavity of the CNTs, followed by the substitution of the inner layers of the CNTs with  $B_2O_3$  in the presence of  $N_2$  gas. Inside the CNTs, boron oxide reacts simultaneously with the gaseous carbon monoxide or the interior layers of the CNTs to produce the boron carbide filling. The final product contained boron carbide filled  $(BN)_x C_y$  nanotubes with an outer layer of pure C and inner layers of pure BN. Fig. 41 shows an illustration of the boron carbide nanowires inside the  $B_xC_yN$  composite tubes. Pure BN tubes filled with boron carbide were also formed in the product.

Nanocables of BN nanotubes filled with Mo clusters are reported by Golberg *et al.*<sup>122</sup> The Mo cluster-filled BN nanotubes are prepared by the treatment of CVD grown CNTs with  $B_2O_3$ , CuO and  $MoO_3$  in a  $N_2$  atmosphere. It has been proposed that the filling of CNTs with  $MoO_3$  precedes the formation of BN tubes on the CNT template. The filling of  $MoO_3$  is then further reduced to metallic Mo by the carbon of the CNTs. Continuous filling of Mo could not be obtained by this method.

BN nanotubes have been used as hosts to oxide materials such as  $\alpha-Al_2O_3$  nanorods.<sup>123</sup> The  $B_4N_3O_2H$  precursor (obtained

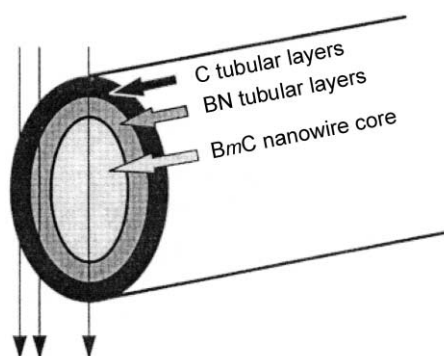


**Fig. 41** Schematic illustration of a multi-phase filled  $B_xC_yN$  nanotube. (Reproduced with permission from ref. 121).

by the thermal decomposition of melamine diborate) when pyrolyzed on  $Si-SiO_2-Al_2O_3$  substrate, yielded  $\alpha-Al_2O_3$  nanorod-filled BN nanocables in abundance.

According to Menon and Srivastava,<sup>124</sup> the chirality of a nanotube directly depends on the tip-end morphology, *i.e.*, for a flat tip end, a zigzag arrangement of the layers in the tube walls is energetically favorable. Rhombohedral stacking in relatively thick BN tubular fibers has been observed,<sup>125</sup> in contrast to the belief that the BN nanotubes are exact analogues of CNTs which usually show random stacking between the layers and no preferential tube helicity. HREM studies of the BN nanotubes reveal layered structures somewhat similar to those in the CNTs (Fig. 42a). However, there are some distinct characteristics. A

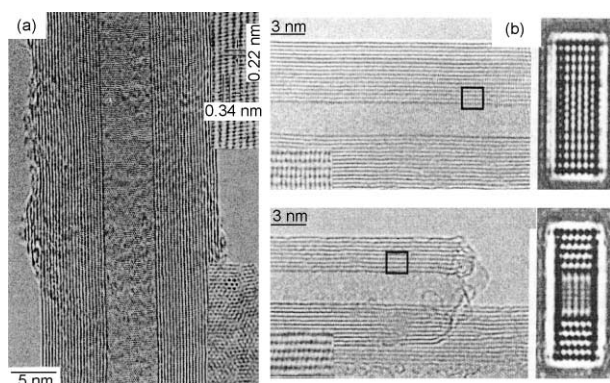


**Fig. 42** (a) A BN nanotube with a uniform layer separation of 0.34 nm. The atomic columns in the wall fragments exhibit layer fringes separated by 0.22 nm and makes an angle of  $12.5^\circ$  with respect to the tube axis, exhibiting *r*-BN stacking; (b) hexagonal stacking and *r*-BN stacking confirmed by the computer-simulated HREM images (right hand side panels). (Reproduced with permission from ref. 120).

field emission high-resolution analytical TEM study has revealed the following characteristic features of the multi-walled BN nanotubes: (i) Hexagonal and rhombohedral (3R) stackings co-exist in nanotube shell assembly, a feature readily seen in HREM images where the layers due to 3R stacking occur in the walls and sometimes in the core besides the regular hexagonal stacking (Fig. 42a). In Fig. 42b the observed HREM images of BN nanotubes are compared with the computer simulated images for the *r*-BN and *h*-BN stacking in the walls. (ii) Flattening of the nanotube cross-section makes clear atomic resolution of the pore structure possible in a three-shelled nanotube. (iii) There is a change in chirality of tubular layers from armchair to zigzag arrangement in a  $30^\circ$  double-walled nanotube kink. BN nanotubes with open tips exhibit local *r*-BN stacking in the walls, while those with close tips exhibit *h*-BN stacking<sup>120</sup> (Fig. 42b).

BN nanotubes obtained by laser ablation and arc-discharge seem to have very few layers and the laser grown tubes self-assemble into long ropes. It is proposed that the growth of BN

nanotubes is due to surface diffusion along the external surface, which also ensures morphological stability of the open end during growth. The nanotube heights are limited by the corresponding diffusion lengths. Recombination of B and N, both in plasma and on the surface, may serve as a possible nucleation center. In the pyrolytically grown BN nanotubes, it is commonly observed that the nanotubes have bulbous tips.<sup>113</sup> The amorphous clusters present in the tip region may play a catalytic role in the nanotube tip-growth process similar to the metal catalyst in the CVD process of CNT growth. Formation of open/flat-tip ends are also observed in some of the BN tubes. There appears to be a preference for the growth of open BN nanotubes in metal oxide-promoted CVD synthesis. One of the reasons behind this may be that the metal atoms occurring at the edges of the growing nanotube may prevent tube closure.<sup>44</sup> Fig. 43 shows the presence of a dark contrast spot on the inner

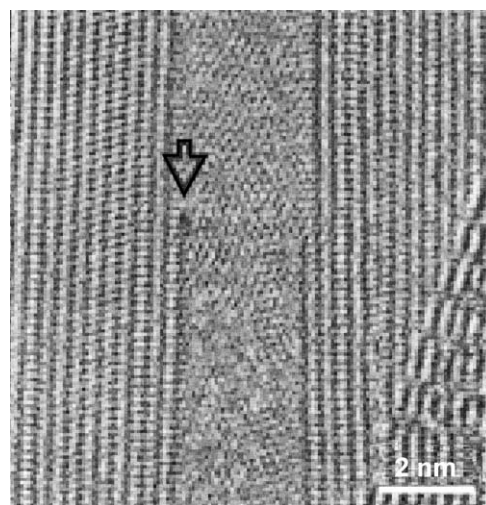


**Fig. 43** The innermost terminated layer of the BN nanotube shows a spot assigned to the Pb atom (or cluster), which may prevent tube closure. (Reproduced with permission from ref. 44).

layer of the tube at the terminated edge. The spot is likely to be related to the presence of the metal atom (Pb) or the metal cluster at that edge, which prevents closure of the layer.

Recently, in their effort to prepare  $Si_3N_4$  nanowires, Gundiah *et al.*<sup>126</sup> have found occasional nanotubes in the TEM images. Similarly, in the preparations of GaN nanowires, GaN nanotubes have been observed by Deepak *et al.*<sup>127</sup>

## 8. Nanotubes of other materials

Transition metal halides such as  $NiCl_2$  crystallize in the  $CdCl_2$  structure, with the metal halide layers held together by weak van der Waals forces.  $NiCl_2$  has been shown to form closed cage structures and nanotubes.<sup>128</sup> These were prepared by heating  $NiCl_2 \cdot 6H_2O$  initially in air to lose the water of crystallization, and then heated further at  $450^\circ C$  under  $N_2$  (Fig. 44).

Very few metallic nanotubes have been synthesized to date. Martin and co-workers<sup>129</sup> have prepared Au nanotubules with lengths upto  $6 \mu m$  and inner diameters of 1 nm by using a pore-wall modified alumina membrane. Co and Fe nanotubules have been synthesized using polycarbonate membranes as templates.<sup>130</sup> Cu and Ni microtubules have also been prepared by the pyrolysis of composite fibers consisting of a poly(ethylene-tetraphthalate) (PET) core fiber and electroless-plated metal skin at the exterior.<sup>131</sup> While Ni microtubules prepared by this method were single-crystalline, the Cu microtubules were polycrystalline. Ordered arrays of Ni nanotubules have been prepared by electrodeposition in the pores of an alumina membrane, the pore walls being modified with an organic amine.<sup>132</sup> Nickel when electrodeposited in the pores binds preferentially to the pore walls because of its strong affinity towards the



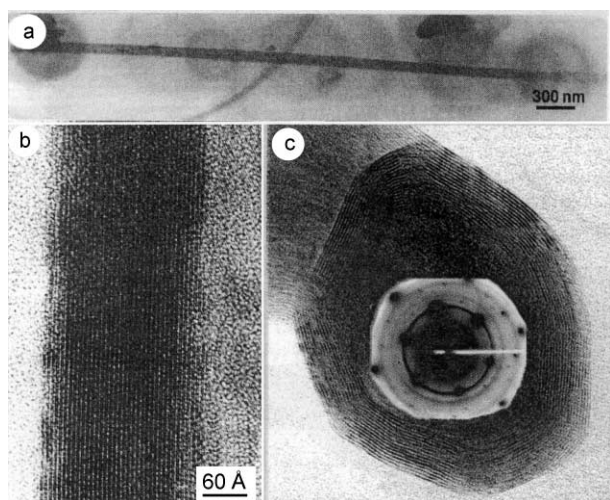


**Fig. 44** (a) Low-magnification view of the  $\text{NiCl}_2$  nanotube; (b) HREM image of the nanotube wall; (c) many-layered cage structure of  $\text{NiCl}_2$ , with the hexagonal ED pattern superimposed. (Reproduced with permission from ref. 128).

amine. In the absence of the amine in the pore walls, solid Ni nanowires were obtained. The alumina membrane could be removed by treatment with NaOH giving highly ordered arrays of Ni nanotubules (Fig. 45a). The Ni nanotubules were ferromagnetic with enhanced coercivity compared to bulk Ni (Fig. 45b).

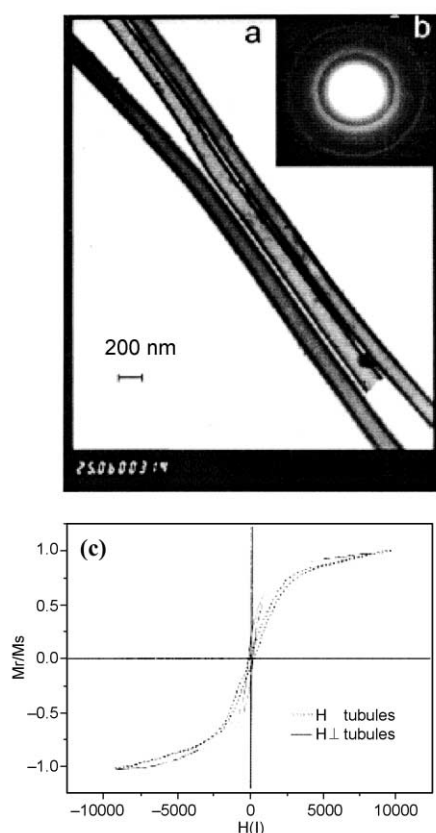


**Fig. 45** (a) TEM image showing the Ni nanotubules; (b) ED pattern of the Ni nanotubules; (c) magnetization vs. applied field ( $M$ - $H$ ) curve showing hysteresis. (Reproduced with permission from ref. 132).

Tellurium nanotubes have been prepared using the polyol method. Orthotelluric acid in ethylene glycol was added to a refluxing solution of ethylene glycol.<sup>133</sup> TEM images taken after stopping the reaction at different stages showed the formation of cylindrical seeds and the subsequent growth of nanotubes along the peripheral edge of the seeds. The walls of the nano-

tubes have a uniform thickness, but appear to be fragile compared to CNTs. Decreasing the amount of the Te precursor in the initial reaction mixture led to the preferential formation of solid nanorods rather than hollow tubes.

## 9. Useful properties of inorganic nanotubes

Various properties of carbon nanotubes of potential technological value are known.<sup>2,134</sup> The properties and applications of the inorganic nanotubes, however, have not been investigated as extensively as would be desirable. The electronic structures of  $\text{MoS}_2$  and  $\text{WS}_2$  have been examined briefly and the semi-conducting nature of the nanotubes confirmed.<sup>55,57a</sup> It is necessary to investigate the optical, electrical and other properties of the various chalcogenide nanotubes. This is especially true of nanotubes of  $\text{NbS}_2$  and such materials which are predicted to be metallic.<sup>57b</sup>  $\text{NbSe}_2$  nanotubes have been found to be metallic at ordinary temperatures, becoming superconducting at lower temperatures.<sup>70</sup> Electronic and optical properties of the BN nanotubes have not yet been investigated in detail. Theoretical calculations suggest BN tubes to be insulating with a wide band gap of 5.5 eV.<sup>13</sup>

Carbon nanotubes have been investigated for  $\text{H}_2$  storage properties.<sup>135</sup> It would be worthwhile to look into the  $\text{H}_2$  storage ability of some of the inorganic nanotubes. The chalcogenide nanotubes with an  $\sim 6$  Å van der Waals gap between the layers, are potential candidates for showing storage capacity. It has been shown recently that BN nanotubes can store a reasonable quantity of  $\text{H}_2$ .<sup>136</sup> Multi-walled BN nanotubes have been shown to possess a capacity of 1.8–2.6 wt% of  $\text{H}_2$  uptake under  $\sim 10$  MPa at room temperature. This value, though smaller than that reported for CNTs, nevertheless suggests the possible use of BN nanotubes as a hydrogen storage system.  $\text{MoS}_2$  nanotubes could be electrochemically charged and discharged with a capacity of 260 mA h  $\text{g}^{-1}$  at 20 °C, corresponding to a formula of  $\text{H}_{1.24}\text{MoS}_2$ .<sup>137</sup> The high storage capacity is believed to be due to the enhanced electrochemical-catalytic activity of the highly nanoporous structure. This may find wide applications in high energy batteries.

Single-walled carbon nanotubes are known to possess extraordinary strength.<sup>138</sup> Mechanical properties of BN nanotubes would be worthy of exploration. Unlike carbon nanotubes, BN nanotubes are predicted to have stable insulating properties independent of their structure and morphology. Thus, BN tubes can be used as nano-insulating devices for encapsulating conducting materials like metallic wires. Filled BN nanotubes are expected to be useful in nanoscale electronic devices and for the preparation of nano-structured ceramics.

Electrochemical studies have been performed with the alkylammonium intercalated  $\text{VO}_x$  nanotubes<sup>139</sup> as well as Mn intercalated  $\text{VO}_x$  nanotubes.<sup>87</sup> Cyclic voltammetry studies of alkylammonium- $\text{VO}_x$  nanotubes showed a single reduction peak, which broadened on replacing the amine with Na with an additional peak. Li ion reactivity has also been tested with Mn- $\text{VO}_x$  nanotubes by reacting with *n*-butyllithium, and found that  $\sim 2$  lithiums per V ion are consumed. Electrochemical Li intercalation of Mn- $\text{VO}_x$  nanotubes show that 0.5 Li ions per V atom were intercalated above 2 V.<sup>87</sup> This observation may be relevant to battery applications.

Conventional microfabricated AFM tips are of limited use for investigating high aspect ratio features (*i.e.* deep and narrow features), mainly because, without special treatment typical aspect ratios of such tips would be around 3 : 1 or lower. Thus, the width of such a tip at a certain height from the apex is much larger than that of the nanotubes of uniform thickness adhered to the tip. The nanotubes therefore would be more suitable for the analysis of deep and narrow structures than the commonly available tips. CNTs have been used as AFM tips and there appears to be every likelihood that extremely narrow structures can be probed.<sup>140</sup>  $\text{WS}_2$  could be mounted on the ultrasharp Si

tip following a similar methodology. These tips were tested in an AFM microscope by imaging a replica of high aspect ratio, and it was observed that these WS<sub>2</sub> nanotube tips provide a considerable improvement in the image quality compared to the conventional ultrasharp Si tips.<sup>141</sup>

The most likely application of the chalcogenide nanotubes is as solid lubricants. Mo and W chalcogenides are widely used as solid lubricants. It has been observed that the hollow nanoparticles of WS<sub>2</sub> show better tribological properties and act as a better lubricant compared to the bulk phase in every respect (friction, wear and life-time of the lubricant).<sup>142</sup> Tribological properties of 2H-MoS<sub>2</sub> and WS<sub>2</sub> powder can be attributed to the weak van der Waals forces between the layers which allow easy shear of the films with respect to each other. The mechanism in the WS<sub>2</sub> nanostructures is somewhat different and the better tribological properties may arise from the rolling friction allowed by the round shape of the nanostructures.

Recently, open-tipped MoS<sub>2</sub> nanotubes were prepared by the decomposition of ball-milled ammonium thiomolybdate powder under a H<sub>2</sub> + thiophene atmosphere, and used as a catalyst for the methanation of CO with H<sub>2</sub>.<sup>143</sup> The conversion of CO to CH<sub>4</sub> was achieved at a much lower temperature compared to polycrystalline MoS<sub>2</sub> particles, and there was no deterioration even after 50 h of consecutive catalyzing cycles. This observation is of importance in the context of energy conversion of global CO<sub>2</sub>.

## 10. Concluding remarks

Inorganic nanotubes have emerged to become a group of novel materials. Although this area of research started with the layered metal chalcogenides, recent results suggest that other inorganic materials can also be prepared in the form of nanotubes, as typified by the metal oxides. It is likely that many new types of inorganic nanotubes will be made in the near future. These would include metal nanotubes as well as nanotubes of inorganic compounds such as Mg<sub>3</sub>B<sub>2</sub>, GeO<sub>2</sub> and GaSe. Theoretical calculations indeed predict a stable nanotubular structure for GaSe.<sup>144</sup> Various layered materials could be explored for this purpose. It is noteworthy that the nanotubes of metal chalcogenides have been made by employing several methods ranging from soft chemical routes to techniques such as arc evaporation and laser ablation (Table 1).

Nanotubes of MoS<sub>2</sub>, WS<sub>2</sub> and a few other layered materials are single-crystalline in the sense that the layers run through the entire structure. Some of the chalcogenide nanotubes are, however, polycrystalline, the nanotubular form being produced by an aggregation of nanoparticles, just as in some of the metal oxide nanotubes.

Properties of inorganic nanotubes such as those of MoS<sub>2</sub> have been investigated to some extent. However, by and large, there is much to be studied with respect to the electronic, optical and other properties of most of the inorganic nanotubes. Properties such as sorption, hydrogen storage and catalytic activity are worthy of exploration. Mechanical properties of BN, B–N–C and related nanotubes are also worthy of study.

## Acknowledgements

The authors thank the Department of Science & Technology and DRDO (India) for support of this research.

## References

- 1 S. Iijima, *Nature*, 1991, **354**, 56.
- 2 C. N. R. Rao, B. C. Satishkumar, A. Govindaraj and M. Nath, *Chem. Phys. Chem.*, 2001, **2**, 78.
- 3 (a) P. Ratnasamy, L. Rodrigues and A. J. Leonard, *J. Phys. Chem.*, 1973, **77**, 2242; (b) J. Wilson and A. D. Yoffe, *Adv. Phys.*, 1969, **269**, 193.
- 4 R. R. Chianelli, E. Prestridge, T. Pecorano and J. P. DeNeufville, *Science*, 1979, **203**, 1105.
- 5 (a) R. Tenne, L. Margulis, M. Genut and G. Hodes, *Nature*, 1992, **360**, 444; (b) L. Margulis, G. Salitra and R. Tenne, *Nature*, 1993, **365**, 113; (c) Y. Feldman, E. Wasserman, D. J. Srolovitch and R. Tenne, *Science*, 1995, **267**, 222.
- 6 (a) C. T. Kresge, M. E. Leonowicz, W. J. Roth, J. C. Vartulli and J. S. Beck, *Nature*, 1992, **259**, 710; (b) J. S. Beck, J. C. Vartulli, W. J. Roth, M. E. Leonowicz, C. T. Kresge, K. D. Schmitt, C. T. W. Chu, D. H. Olson, E. W. Sheppard, S. B. McCullen, J. B. Higgins and J. C. Scwenker, *J. Am. Chem. Soc.*, 1992, **114**, 10834.
- 7 G. R. Pratzke, F. Krumeich and R. Nesper, *Angew. Chem., Int. Ed.*, 2002, **41**, 2446.
- 8 (a) W. Stöber, A. Fink and E. Bohn, *J. Colloid Interface Sci.*, 1968, **26**, 62; (b) M. Nakamura and Y. Matsui, *J. Am. Chem. Soc.*, 1995, **117**, 2651.
- 9 P. M. Ajayan, O. Stephane, Ph. Redlich and C. Colliex, *Nature*, 1995, **375**, 564.
- 10 (a) B. C. Satishkumar, A. G. Govindaraj, E. M. Vogl, L. Basumallick and C. N. R. Rao, *J. Mater. Res.*, 1997, **12**, 604; (b) B. C. Satishkumar, A. Govindaraj, M. Nath and C. N. R. Rao, *J. Mater. Chem.*, 2000, **10**, 2115.
- 11 M. E. Spahr, P. Bitterli, R. Nesper, M. Müller, F. Krumeich and H. U. Nissen, *Angew. Chem., Int. Ed.*, 1998, **37**, 1263 (*Angew. Chem.*, 1998, **110**, 1339).
- 12 L. Pu, X. Bao, J. Zou and D. Feng, *Angew. Chem., Int. Ed.*, 2001, **40**, 1490.
- 13 (a) M. L. Cohen, *Solid State Commun.*, 1994, **92**, 45; (b) J. L. Corkill and M. L. Cohen, *Phys. Rev. B*, 1994, **49**, 5081; (c) Y. Miyamoto, A. Rubio, S. G. Louie and M. L. Cohen, *Phys. Rev. B*, 1994, **50**, 18360.
- 14 (a) K. Kobayashi and N. Kurita, *Phys. Rev. Lett.*, 1993, **70**, 3542; (b) Z. W. Sieh, K. Cherrey, N. G. Chopra, X. Blasé, Y. Miyamoto, A. Rubio, M. L. Cohen, S. G. Louie, A. Zettl and P. Gronsky, *Phys. Rev. B*, 1994, **51**, 11229.
- 15 (a) R. Sen, B. C. Satishkumar, A. Govindaraj, K. R. Harikumar, G. Raina, J. P. Zhang, A. K. Cheetham and C. N. R. Rao, *Chem. Phys. Lett.*, 1998, **287**, 671; (b) O. Stephan, P. M. Ajayan, C. Colliex, Ph. Redlich, J. M. Lambert, P. Bernier and P. Lefing, *Science*, 1994, **266**, 1683.
- 16 (a) P. Gleize, M. C. Schouler, P. Gabelle and M. Caillet, *J. Mater. Sci.*, 1994, **29**, 1575; (b) O. R. Lourie, C. R. Jones, B. M. Bertlett, P. C. Gibbons, R. S. Ruoff and W. E. Buhro, *Chem. Mater.*, 2000, **12**, 1808; (c) R. Ma, Y. Bando and T. Sato, *Chem. Phys. Lett.*, 2001, **337**, 61.
- 17 F. L. Deepak, C. P. Vinod, K. Mukhopadhyay, A. Govindaraj and C. N. R. Rao, *Chem. Phys. Lett.*, 2002, **353**, 345.
- 18 C. N. R. Rao and A. G. Govindaraj, *Acc. Chem. Res.*, 2002 and references therein.
- 19 R. Tenne, M. Homyonfer and Y. Feldman, *Chem. Mater.*, 1998, **10**, 3225 and references therein.
- 20 (a) M. Hershfinkel, L. A. Gheber, V. Volterra, J. L. Hutchison, L. Margulis and R. Tenne, *J. Am. Chem. Soc.*, 1994, **116**, 1914; (b) T. Tsirlina, Y. Feldman, M. Homyonfer, J. Sloan, J. L. Hutchison and R. Tenne, *Fullerene Sci. Technol.*, 1998, **6**, 157.
- 21 M. Nath, A. Govindaraj and C. N. R. Rao, *Adv. Mater.*, 2001, **13**, 283.
- 22 M. Nath and C. N. R. Rao, *Chem. Commun.*, 2001, 2236.
- 23 M. Nath and C. N. R. Rao, *J. Am. Chem. Soc.*, 2001, **123**, 4841.
- 24 M. Nath and C. N. R. Rao, *Angew. Chem., Int. Ed.*, 2002, **41**, 3451.
- 25 A. P. Lin, C. Y. Mou and S. D. Liu, *Adv. Mater.*, 2000, **12**, 103.
- 26 J. Zhang, L. Sun, C. Liao and C. Yan, *Chem. Commun.*, 2002, 262.
- 27 M. Niederberger, H.-J. Muhr, F. Krumeich, F. Bieri, D. Günther and R. Nesper, *Chem. Mater.*, 2000, **12**, 1995.
- 28 C. N. R. Rao, A. G. Govindaraj, F. L. Deepak, N. A. Gunari and M. Nath, *Appl. Phys. Lett.*, 2001, **78**, 1853.
- 29 T. Kasuga, M. Hiramatsu, A. Hason, T. Sekino and K. Niihara, *Langmuir*, 1998, **14**, 3160.
- 30 C. N. R. Rao, B. C. Satishkumar and A. Govindaraj, *Chem. Commun.*, 1997, 1581.
- 31 C. M. Zelenski and P. K. Dorhout, *J. Am. Chem. Soc.*, 1998, **120**, 734.
- 32 A. Loiseau, F. Williams, N. Demoncey, G. Hug and H. Pascard, *Phys. Rev. Lett.*, 1996, **76**, 4737.
- 33 M. Homyonfer, Y. Mastai, M. Hershfinkel, V. Volterra, J. L. Hutchison and R. Tenne, *J. Am. Chem. Soc.*, 1996, **118**, 7804.
- 34 Y. Feldman, G. L. Frey, M. Homyonfer, V. Lyakhovitskaya, L. Margulis, H. Cohen, G. Hodes, J. L. Hutchison and R. Tenne, *J. Am. Chem. Soc.*, 1996, **118**, 5362.



- 35 M. Homyonfer, B. Alpersen, Y. Rosenberg, L. Sapir, S. R. Cohen, G. Hodes and R. Tenne, *J. Am. Chem. Soc.*, 1997, **119**, 2693.
- 36 S. P. Cramer, K. S. Liang, A. J. Jacobson, C. H. Chang and R. R. Chianelli, *Inorg. Chem.*, 1984, **23**, 1215.
- 37 G. U. Kulkarni and C. N. R. Rao, *Catal. Lett.*, 1991, **11**, 63.
- 38 (a) E. Diemann and A. Müller, *Coord. Chem. Rev.*, 1973, **10**, 79; (b) R. R. Chianelli and M. B. Dines, *Inorg. Chem.*, 1978, **17**, 2758; (c) A. Wildervanck and F. Jelinek, *Z. Anorg. Allg. Chem.*, 1964, **328**, 309.
- 39 (a) C. N. R. Rao and K. P. R. Pisharody, *Prog. Solid State Chem.*, 1976, **10**, 207; (b) N. Allali, V. Gaborit, E. Prouzet, C. Geantet, M. Danot and A. Nadiri, *J. Phys. IV (France)*, 1997, **7**, C2-927; (c) E. Bjerkelund and A. Kjekhus, *Z. Anorg. Allg. Chem.*, 1964, **328**, 235; (d) F. K. McTaggart and A. D. Wadsley, *Aust. J. Chem.*, 1958, **11**, 445.
- 40 M. Nath, K. Mukhopadhyay and C. N. R. Rao, *Chem. Phys. Lett.*, 2002, **352**, 163.
- 41 (a) Y. Q. Zhu, W. K. Hsu, M. Terrones, S. Firth, N. Grobert, R. J. H. Clark, H. W. Kroto and D. R. M. Walton, *Chem. Commun.*, 2001, 121; (b) Y. Q. Zhu, W. K. Hsu, M. Terrones, S. Firth, N. Grobert, R. J. H. Clark, H. W. Kroto and D. R. M. Walton, *Chem. Phys. Lett.*, 2001, **342**, 15.
- 42 W. K. Hsu, Y. Q. Zhu, N. Yao, S. Firth, R. J. H. Clark, H. W. Kroto and D. R. M. Walton, *Adv. Funct. Mater.*, 2001, **11**, 69.
- 43 W. K. Hsu, Y. Q. Zhu, C. B. Bothroyd, I. Kinlöch, S. Trasobares, H. Terrones, N. Grobert, M. Terrones, R. Escudero, G. Z. Chen, C. Colliex, A. H. Windle, D. H. Fray, H. W. Kroto and D. R. M. Walton, *Chem. Mater.*, 2000, **12**, 3541.
- 44 D. Golberg and Y. Bando, *Appl. Phys. Lett.*, 2001, **79**, 415.
- 45 (a) R. L. D. Whitby, W. K. Hsu, C. B. Bothroyd, P. K. Fearon, H. W. Kroto and D. R. M. Walton, *Chem. Phys. Chem.*, 2001, **10**, 620; (b) R. L. D. Whitby, W. K. Hsu, P. K. Fearon, N. C. Billingham, I. Maurin, H. W. Kroto, D. R. M. Walton, C. B. Bothroyd, S. Firth, R. J. H. Clark and D. Collison, *Chem. Mater.*, 2002, **14**, 2209; (c) R. L. D. Whitby, W. K. Hsu, P. C. P. Watts, H. W. Kroto and D. R. M. Walton, *Appl. Phys. Lett.*, 2001, **79**, 4574; (d) W. K. Hsu, Y. Q. Zhu, H. W. Kroto, D. R. M. Walton, R. Kamalakaran and M. Terrones, *Appl. Phys. Lett.*, 2000, **77**, 4130.
- 46 Y. Q. Zhu, W. K. Hsu, H. W. Kroto and D. R. M. Walton, *Chem. Commun.*, 2001, 2184.
- 47 Y. Q. Zhu, W. K. Hsu, H. Terrones, N. Grobert, B. H. Chang, M. Terrones, B. Q. Wei, H. W. Kroto, D. R. M. Walton, C. B. Bothroyd, I. Kinlöch, G. Z. Chen, A. H. Windle and D. J. Fray, *J. Mater. Chem.*, 2000, **10**, 2570.
- 48 Y. Q. Zhu, W. K. Hsu, N. Grobert, B. H. Chang, M. Terrones, H. Terrones, H. W. Kroto and D. R. M. Walton, *Chem. Mater.*, 2000, **12**, 1190.
- 49 N. Grobert, M. Terrones, A. J. Osborne, H. Terrones, W. K. Hsu, S. Trasobares, Y. Q. Zhu, J. P. Hare, H. W. Kroto and D. R. M. Walton, *Appl. Phys. A*, 1998, **69**, 595.
- 50 J. Sloan, J. L. Hutchison, R. Tenne, Y. Feldman, T. Srilina and M. Homyonfer, *J. Solid State Chem.*, 1999, **144**, 100.
- 51 M. Rémskar, Z. Skraba, C. Ballif, R. Sanjines and F. Levy, *Surf. Sci.*, 1999, **435**, 637.
- 52 M. Homyonfer, Y. Feldman, L. Margulis and R. Tenne, *Fullerene Sci. Technol.*, 1998, **6**, 59.
- 53 (a) S. Iijima, S. Ichihashi and Y. Ando, *Nature*, 1992, **356**, 776; (b) D. E. H. Jones, *Nature*, 1991, **351**, 526; (c) S. Iijima, P. M. Ajayan and T. Ichihashi, *Phys. Rev. Lett.*, 1991, **69**, 3900.
- 54 R. Tenne, *Adv. Mater.*, 1995, **7**, 965.
- 55 G. Seifert, H. Terrones, M. Terrones, G. Jungnickel and T. Frauenheim, *Phys. Rev. Lett.*, 2000, **85**, 146.
- 56 G. Seifert, T. Köhler and R. Tenne, *J. Phys. Chem. B*, 2002, **106**, 2497.
- 57 (a) G. Seifert, H. Terrones, M. Terrones, G. Jungnickel and T. Frauenheim, *Solid State Commun.*, 2000, **114**, 245; (b) G. Seifert, H. Terrones, M. Terrones, G. Jungnickel and T. Frauenheim, *Solid State Commun.*, 2000, **115**, 635.
- 58 C. Thomazeau, C. Geantet, M. Lacroix, V. Harlé, S. Benazeth, C. Marhic and M. Danot, *J. Solid State Chem.*, 2001, **160**, 147.
- 59 A. Zak, Y. Feldman, Y. Alperovich, R. Rosentsveig and R. Tenne, *J. Am. Chem. Soc.*, 2000, **122**, 11108.
- 60 (a) P. J. F. Harris, in *Carbon Nanotube and Related Structures*, Cambridge University Press, UK, 1999 pp. 62–107; (b) S. Amelinckx, D. Bernaerts, X. B. Zhang, G. Van Tendeloo and J. Van Landuyt, *Science*, 1995, **267**, 1334; (c) A. Oberlin, M. Endo and T. Kayama, *J. Cryst. Growth*, 1992, **32**, 6941; (d) H. Dai, A. Z. Rinzler, P. Nikolaev, A. Thess, D. T. Colbert and R. E. Smalley, *Chem. Phys. Lett.*, 1996, **260**, 471.
- 61 W. K. Hsu, B. H. Chang, Y. Q. Zhu, W. Q. Han, H. Terrones, M. Terrones, N. Grobert, A. K. Cheetham, H. W. Kroto and D. R. M. Walton, *J. Am. Chem. Soc.*, 2000, **122**, 10155.
- 62 P. Afanasiev, C. Geantet, C. Thomazeau and B. Jouget, *Chem. Commun.*, 2000, 1001.
- 63 M. Remskar, A. Mrzel, Z. Skraba, A. Jesih, M. Ceh, J. Demšar, P. Stadelmann, F. Lévy and D. Mihailovic, *Science*, 2001, **292**, 479.
- 64 R. Sen, A. Govindaraj, K. Suenaga, S. Suzuki, H. Kataura, S. Iijima and Y. Achiba, *Chem. Phys. Lett.*, 2001, **340**, 242.
- 65 D. H. Galván, R. Rangel and G. Alonso, *Fullerene Sci. Technol.*, 1998, **6**, 1025.
- 66 H. D. Flack, *J. Appl. Crystallogr.*, 1972, **5**, 138.
- 67 D. L. Greenaway and R. Nitsche, *J. Phys. Chem. Solids*, 1965, **26**, 1445.
- 68 M. I. Nathan, M. W. Shafer and J. E. Smith, *Bull. Am. Phys. Soc.*, 1972, **17**, 336.
- 69 D. H. Galván, J.-H. Kim, M. B. Maple, M. Avalos-Berja and E. Adem, *Fullerene Sci. Technol.*, 2000, **8**, 143.
- 70 M. Nath S. Kar A. K. Raychaudhuri C. N. R. Rao, *Chem. Phys. Lett.*, in press.
- 71 C. Schuffenhauer, R. P-Biro and R. Tenne, *J. Mater. Chem.*, 2002, **12**, 1587.
- 72 (a) C. S. Wang and J. M. Chen, *Solid State Commun.*, 1974, **14**, 1145; (b) A. LeBlanc-Soreau, P. Molinié and E. Faulques, *Physica C*, 1997, **282–287**, 1937.
- 73 R. F. Frindt, *Phys. Rev. Lett.*, 1972, **28**, 299.
- 74 Y. Wu, B. Messer and P. Yang, *Adv. Mater.*, 2001, **13**, 1487.
- 75 A. Govindaraj, F. L. Deepak, N. A. Gunari and C. N. R. Rao, *Israel J. Chem.*, 2001, **41**, 23.
- 76 P. V. Teredesai, F. L. Deepak, A. Govindaraj, C. N. R. Rao and A. K. Sood, *J. Nanosci. Nanotechnol.*, 2002, **2**, 495.
- 77 L. Dloczik, R. Engelhardt, K. Ernst, S. Fiechter, I. Seiber and R. Könenkamp, *Appl. Phys. Lett.*, 2001, **78**, 3687.
- 78 X. Ziang, Y. Xie, L. Zhu, W. He and Y. Qian, *Adv. Mater.*, 2001, **13**, 1278.
- 79 Y. Peng, Z. Meng, C. Zhong, J. Lu, L. Xu, S. Zhang and Y. Qian, *New J. Chem.*, 2001, **25**, 1359.
- 80 H. Imai, Y. Takei, K. Shimizu, M. Matsuda and H. Hirashima, *J. Mater. Chem.*, 1999, **9**, 2971.
- 81 H. G. Bachmann, F. R. Ahmed and W. H. Barnes, *Z. Kristallogr.*, 1961, **115**, 110.
- 82 R. Enjalbert and J. Galy, *Acta Crystallogr., Sect. C*, 1986, **42**, 1467.
- 83 J. Galy, *J. Solid State Chem.*, 1992, **100**, 229.
- 84 M. S. Whittingham, J. Guo, R. Chen, T. Chirayil, G. Janauer and P. Y. Zavalji, *Solid State Ionics*, 1995, **75**, 257.
- 85 F. Krumeich, H.-J. Muhr, M. Niederberger, F. Bieri, B. Schnyder and R. Nesper, *J. Am. Chem. Soc.*, 1999, **121**, 8324.
- 86 H.-J. Muhr, F. Krumeich, U. P. Schönholzer, F. Bieri, M. Niederberger, L. J. Gauckler and R. Nesper, *Adv. Mater.*, 2000, **12**, 231.
- 87 A. Doble, K. Ngala, S. Yang, P. Y. Zavalji and M. S. Whittingham, *Chem. Mater.*, 2001, **13**, 4382.
- 88 P. Hoyer, *Langmuir*, 1996, **12**, 1411.
- 89 R. A. Caruso, J. H. Schattka and A. Greiner, *Adv. Mater.*, 2001, **13**, 1577.
- 90 D. Gong, C. A. Grimes, O. K. Varghese, W. Hu, R. S. Singh, Z. Chen and E. C. Dickey, *J. Mater. Res.*, 2001, **16**, 3331.
- 91 S. M. Liu, L. M. Gan, L. H. Liu, W. D. Zhang and H. C. Zeng, *Chem. Mater.*, 2002, **14**, 1391.
- 92 M. Zhang, Y. Bando and K. Wada, *J. Mater. Res.*, 2001, **16**, 1408.
- 93 (a) H. Nakamura and Y. Matsui, *J. Am. Chem. Soc.*, 1995, **117**, 2651; (b) H. Nakamura and Y. Matsui, *Adv. Mater.*, 1995, **7**, 871.
- 94 (a) M. Harada and M. Adachi, *Adv. Mater.*, 2000, **12**, 839; (b) M. Adachi, T. Harada and M. Harada, *Langmuir*, 1999, **15**, 7079.
- 95 L. Wang, S. Tomura, F. Ohashi, M. Maeda, M. Suzuki and K. Inukai, *J. Mater. Chem.*, 2001, **11**, 1465.
- 96 Y. Zhang and A. Reller, *Chem. Commun.*, 2002, 606.
- 97 H. J. Chang, Y. F. Chen, H. P. Lin and C. Y. Mou, *Appl. Phys. Lett.*, 2001, **78**, 3791.
- 98 J. Zou, L. Pu, X. Bao and D. Feng, *Appl. Phys. Lett.*, 2002, **80**, 1079.
- 99 J. Zhang, L. Sun, C. Liao and C. Yan, *Chem. Commun.*, 2002, 262.
- 100 M. Yada, M. Mihara, S. Mouri, M. Kuroki and T. Kijima, *Adv. Mater.*, 2002, **14**, 309.
- 101 B. Cheng and E. T. Samulski, *J. Mater. Chem.*, 2001, **11**, 2901.
- 102 B. A. Hernandez, K.-S. Chang, E. R. Fisher and P. K. Dorhout, *Chem. Mater.*, 2002, **14**, 480.
- 103 X. Blase, A. Rubio, S. G. Louie and M. L. Cohen, *Europhys. Lett.*, 1994, **28**, 335.
- 104 N. G. Chopra, R. G. Luyken, K. Cherrey, V. H. Crespi, M. L. Cohen, S. G. Louie and A. Zettl, *Science*, 1995, **269**, 966.
- 105 O. Stephan, Y. Bando, A. Loiseau, F. Williams, N. Schramechenko, T. Tamiya and T. Sato, *Appl. Phys. A: Mater. Sci. Process.*, 1998, **67**, 107.

- 106 M. Terrones, W. K. Hsu, H. Terrones, J. P. Zhang, S. Ramos, J. P. Hare, R. Castillo, K. Prassides, A. K. Cheetham, H. W. Kroto and D. R. M. Walton, *Chem. Phys. Lett.*, 1996, **259**, 568.
- 107 (a) D. P. Yu, X. S. Sun, C. S. Lee, I. Bello, S. T. Lee, H. D. Gu, K. M. Leung, G. W. Zhou, Z. F. Dong and Z. Zhang, *Appl. Phys. Lett.*, 1998, **72**, 1966; (b) G. W. Zhou, Z. Zhang, Z. G. Bai and D. P. Yu, *Solid State Commun.*, 1999, **109**, 555; (c) M. Terauchi, M. Tanaka, H. Matsuda, M. Takeda and K. Kimura, *J. Electron Microsc.*, 1997, **1**, 75.
- 108 T. Laude, Y. Matsui, A. Marraud and B. Jouffrey, *Appl. Phys. Lett.*, 2000, **76**, 3239.
- 109 (a) D. Golberg, Y. Bando, W. Han, K. Kurashima and T. Sato, *Chem. Phys. Lett.*, 1999, **308**, 337; (b) P. W. Fowler, K. M. Rogers, G. Seifert, M. Terrones and H. Terrones, *Chem. Phys. Lett.*, 1999, **299**, 359.
- 110 E. Bengu and L. D. Marks, *Phys. Rev. Lett.*, 2001, **86**, 2385.
- 111 Y. Shimizu, Y. Moriyoshi, H. Tanaka and S. Komatsu, *Appl. Phys. Lett.*, 1999, **75**, 929.
- 112 Y. Chen, L. T. Chadderton, J. F. Gerals and J. S. Williams, *Appl. Phys. Lett.*, 1999, **74**, 2960.
- 113 R. Ma, Y. Bando, T. Sato and K. Kurashima, *Chem. Mater.*, 2001, **13**, 2965.
- 114 C. C. Tang, M. L. de la Chapelle, P. Li, Y. M. Liu, H. Y. Dang and S. S. Fan, *Chem. Phys. Lett.*, 2001, **342**, 492.
- 115 C. C. Tang, Y. Bando, T. Sato and K. Kurashima, *Chem. Commun.*, 2002, 1290.
- 116 K. B. Shelimov and M. Moskovits, *Chem. Mater.*, 2000, **12**, 250.
- 117 (a) W. Han, Y. Bando, K. Kurashima and T. Sato, *Appl. Phys. Lett.*, 1998, **73**, 3085; (b) D. Golberg, W. Han, Y. Bando, L. Burgeois, K. Kurashima and T. Sato, *J. Appl. Phys.*, 1999, **86**, 2364; (c) D. Golberg, Y. Bando, K. Kurashima and T. Sato, *Chem. Phys. Lett.*, 2000, **323**, 185.
- 118 D. Golberg, Y. Bando, K. Kurashima and T. Sato, *Solid State Commun.*, 2000, **116**, 1.
- 119 Y. Zhang, K. Suenaga, C. Colliex and S. Iijima, *Science*, 1998, **281**, 973.
- 120 W. Han, Ph. K.-Redlich, F. Ernst and M. Rühle, *Appl. Phys. Lett.*, 1999, **75**, 1875.
- 121 W. Han, P. K. -Redlich, F. Ernst and M. Rühle, *Chem. Mater.*, 1999, **11**, 3620.
- 122 D. Golberg, Y. Bando, K. Kurashima and T. Sato, *J. Nanosci. Nanotechnol.*, 2000, **1**, 49.
- 123 R. Ma, Y. Bando and T. Sato, *Adv. Mater.*, 2002, **14**, 366.
- 124 M. Menon and D. Srivastava, *Chem. Phys. Lett.*, 1999, **307**, 407.
- 125 L. Burgeois, Y. Bando and T. Sato, *J. Phys. D: Appl. Phys.*, 2000, **33**, 1902.
- 126 G. Gundiah, G. V. Madhav, A. Govindaraj, Md. Motin Seikh and C. N. R. Rao, *J. Mater. Chem.*, 2002, **12**, 1606.
- 127 F. L. Deepak, A. Govindaraj and C. N. R. Rao, *J. Nanosci. Nanotechnol.*, 2001, **1**, 303.
- 128 Y. R. Hachohen, E. Grunbaum, R. Tenne, J. Sloan and J. L. Hutchison, *Nature*, 1998, **395**, 337.
- 129 (a) C. R. Martin, M. Nishizawa, K. Jirage and M. Kang, *J. Phys. Chem. B*, 2001, **105**, 1925; (b) J. C. Hutleen, K. B. Jirage and C. R. Martin, *J. Am. Chem. Soc.*, 2000, **120**, 6603; (c) C. J. Brumlik and C. R. Martin, *J. Am. Chem. Soc.*, 1991, **113**, 3174.
- 130 G. Tourillon, L. Pontonnier, J. P. Levy and V. Langlais, *Electrochem. Solid-State Lett.*, 2000, **3**, 20.
- 131 C. C. Han, M. Y. Bai and J. T. Lee, *Chem. Mater.*, 2001, **13**, 4260.
- 132 J. Bao, C. Tie, Z. Xu, Q. Zhou, D. Shen and Q. Ma, *Adv. Mater.*, 2001, **13**, 1631.
- 133 B. Mayers and Y. Xia, *Adv. Mater.*, 2002, **14**, 279.
- 134 (a) S. Saito, S. I. Sawada, M. Hawada and A. Oshima, *Mater. Sci. Eng.*, 1993, **B19**, 105; (b) R. Saito, M. Fujita, G. Dresslhaus and M. S. Dresslhaus, *Mater. Sci. Eng.*, 1993, **B19**, 185; (c) R. Dagani, *Chem. Eng. News*, Jan 11 1999, 31.
- 135 (a) H. M. Cheng, Q. H. Yang and C. Liu, *Carbon*, 2001, **39**, 1447; (b) P. Hou, Q. Yang, S. Bai, S. Xu, M. Liu and H. Cheng, *J. Phys. Chem. B*, 2002, **106**, 963 and references therein.
- 136 R. Ma, Y. Bando, H. Zhu, T. Sato, C. Xu and D. Wu, *J. Am. Chem. Soc.*, 2002, **124**, 7672.
- 137 J. Chen, N. Kuriyama, H. Yuan, H. T. Takeshita and T. Sakai, *J. Am. Chem. Soc.*, 2001, **123**, 11813.
- 138 (a) M. Treacy and T. Ebbesen, *Nature*, 1996, **381**, 678; (b) C. F. Cornwell and L. T. Wille, *Solid State Commun.*, 1997, **101**, 505.
- 139 M. E. Spahr, P. S. Bitterli, R. Nesper, O. Haas and P. Novak, *J. Electrochem. Soc.*, 1999, **146**, 2780.
- 140 H. Dai, J. Hafner, A. G. Rinzler, D. T. Colbert and R. E. Smalley, *Nature*, 1996, **384**, 147.
- 141 A. Rothschild, S. R. Cohen and R. Tenne, *Appl. Phys. Lett.*, 1999, **75**, 4025.
- 142 L. Rapoport, Y. Bilik, Y. Feldman, M. Homyonfer, S. R. Cohen and R. Tenne, *Nature*, 1997, **387**, 791.
- 143 J. Chen, S. L. Li, Q. Xu and K. Tanaka, *Chem. Commun.*, 2002, 1722.
- 144 M. Cote and M. L. Cohen, *Phys. Rev. B*, 1998, **58**, R2477.